Materials Science & Engineering A 948 (2025) 149269

Contents lists available at ScienceDirect

Materials Science & Engineering A

journal homepage: www.elsevier.com/locate/msea

Inconel 718 fabricated *via* arc-based directed energy deposition assisted with *in situ* interlayer hot forging

Francisco Werley Cipriano Farias [a,b,*], Valdemar Rebelo Duarte [b,c], João da Cruz Payão Filho [a], Norbert Schell [d], Emad Maawad [d], Jonathan Cormier [e], Fabio Machado Alves da Fonseca [e,1], Antonio J. Ramirez [f], Telmo Jorge Gomes dos Santos [b,c], J.P. Oliveira [b,g,**]

[a] *Programa de Engenharia Metalúrgica e de Materiais, Universidade Federal do Rio de Janeiro, 21941-972, Rio de Janeiro, Brazil*
[b] *UNIDEMI, Department of Mechanical and Industrial Engineering, NOVA School of Science and Technology, Universidade NOVA de Lisboa, 2829-516, Caparica, Portugal*
[c] *Laboratório Associado de Sistemas Inteligentes, LASI, 4800-058, Guimarães, Portugal*
[d] *Helmholtz-Zentrum Hereon, Institute of Materials Physics, Max-Planck-Str. 1, 21502, Geesthacht, Germany*
[e] *Institut Pprime, UPR CNRS 3346, Physics and Mechanics of Materials Department, ISAE-ENSMA, 1 Avenue Clément Ader, BP 40109, Futuroscope, 86961, Chasseneuil, France*
[f] *Ohio State University – Department of Materials Science and Engineering, Columbus, OH, USA*
[g] *CENIMAT|i3N, Department of Materials Science, School of Science and Technology, NOVA University, Lisbon, Caparica, Portugal*

ARTICLE INFO

Keywords:
Additive manufacturing
Grain size refinement
Interlayer mechanical deformation
Inconel
Elevated temperature tensile test

ABSTRACT

Ni-based superalloys fabricated by arc-based directed energy deposition (DED) typically exhibit a non-optimized microstructure, characterized by coarse and oriented columnar grains, which limits their performance and industrial applications. In this context, microstructure refinement techniques previously applied to arc-based welding have been tested in additive manufacturing, highlighting interlayer mechanical deformation methods (*e.g.*, rolling and peening). The present work describes the grain size refinement mechanism of *in situ* interlayer hot forging (HF) and evaluates its effect on the elevated-temperature tensile behavior of Inconel 718 fabricated *via* DED (IN718 DED). HF induced a dynamically recrystallized zone (~1 mm) on the top layer surface and a deformed zone (~0.5 mm) immediately beneath it, which was not completely remelted by the subsequent layer deposition, thereby generating recrystallized grains during subsequent multiple thermal cycles. During the homogenization heat treatment, the remaining deformed region recrystallized, generating a finer grain size and an almost equiaxed microstructure. HF also improves the yield strength at elevated-temperatures and induces an almost isotropic behavior. For the first time, enabling the IN718 DED to meet the grain size, elongation, and elevated-temperature yield strength requirements (AMS 5662).

1. Introduction

Parts fabricated *via* fusion-based metal additive manufacturing (AM) processes, *e.g.*, directed energy deposition (DED), typically exhibit a coarse and oriented microstructure, a tendency especially notable for Ni-based superalloys and austenitic stainless steels (no solid-state allotropic transformations) [1–8]. These microstructure aspects can hinder the use of parts fabricated *via* DED (*e.g.*, welding-based) in critical applications, as the grain size and mechanical properties requirements are usually not met (*e.g.*, AMS 5662) [9]. Such a non-optimized microstructure arises from thermal conditions during solidification [10,11], where a localized heat source induces an intense thermal gradient in the melt pool, inhibiting the columnar-to-equiaxed transition [12,13]. Additionally, epitaxial grain growth is promoted by the layer-by-layer printing strategy and almost unidirectional heat flux, leading to a coarse and highly oriented primary microstructure [14].

In high-energy density AM processes (*e.g.*, laser powder bed fusion, L-PBF), the coarse and oriented microstructure issues observed in Ni-based superalloys can be partially mitigated through the mandatory post-deposition heat treatments (PDHT), which can promote static

* Corresponding author. Programa de Engenharia Metalúrgica e de Materiais, Universidade Federal do Rio de Janeiro, 21941-972, Rio de Janeiro, Brazil.
** Corresponding author. CENIMAT|i3N, Department of Materials Science, School of Science and Technology, NOVA University, Lisbon, Caparica, Portugal
E-mail addresses: fw.farias@campus.fct.unl.pt (F.W.C. Farias), jp.oliveira@fct.unl.pt (J.P. Oliveira).
[1] Now at NAAREA, Nanterre, France.

https://doi.org/10.1016/j.msea.2025.149269
Received 9 May 2025; Received in revised form 8 October 2025; Accepted 12 October 2025
Available online 27 October 2025

recrystallization [15,16]. Otherwise, this straightforward solution usually does not apply to low-density energy AM processes, *e.g.*, gas metal arc-based DED, where notorious grain boundary migration is not typically observed during PDHT [2,9,17–24]. For the specific case of Inconel 718 (a precipitation-strengthened Ni-based superalloy) fabricated *via* arc-based DED, another process limitation is its high susceptibility to hot cracking (solidification and liquation) [3,25–28]. As a result, controlling the microstructure by optimizing deposition parameters becomes restricted due to the narrow process window. Therefore, it is a challenge to achieve a fine and non-oriented microstructure and meet the rigid materials requirements (*e.g.*, AMS 5662) for Ni-based superalloy fabricated by arc-based DED (*e.g.*, Inconel 718) [24].

Methodologies previously developed for welding/casting to refine the microstructure have also been tested in arc-based DED, which include inoculants [29–32], interlayer mechanical deformation (IMD) [5,20,33–36], and thermal management [37,38]. IMD stands out because it does not alter the feedstock material composition, can be applied to all weldable materials, and promotes a refined microstructure [34,39–41]. IMD systems can be categorized based on temperature (hot or cold) and type of deformation (quasi-static – rolling – and dynamic –hammering/forging/peening) [20]. Among these, cold/warm/hot rolling and cold peening were applied to Inconel 718 fabricated by DED (laser- and arc-based) [19,42–44]. Arc-based DED + interlayer warm rolling [19] effectively refined the Inconel 718 primary microstructure, leading to significant improvements in elevated-temperature tensile strength in relation to conditions without interlayer rolling. However, quasi-static IMD presents a limited path planning flexibility (lower curvature radius trajectories), which contradicts the additive manufacturing process principle. In contrast, dynamic IMD can be integrated with the DED printer [40,45], overcoming the aforementioned limitation. In relation to dynamic IMD processes, the prototype developed by Duarte et al. [40,46] (*in situ* interlayer hot forging, HF) is particularly noteworthy. It utilizes a co-axial deformation/deposition tool to deposit and simultaneously forge the freshly deposited material (*i.e.*, hot deformation), thereby minimizing the path planning restrictions associated with interlayer rolling (robust and rigid equipment) and peening/hammering (dedicated deformation unit). In addition, hot deformation reduces the idle time (part cooling) compared to cold deformation IMD processes, which enhances the process efficiency [37].

Due to the different deformation modes and operational temperatures, the grain size refinement mechanism promoted by IMD and its effect on the mechanical behavior of printed parts have not been fully elucidated, particularly for Ni-based superalloys fabricated by DED [39,42,43,47–50]. In this regard, the present work aims to: (i) describe the grain size refinement promoted by *in situ* interlayer hot forging (HF) and (ii) evaluate the effects of HF on microstructure and elevated-temperature tensile behavior of Inconel 718 fabricated by arc-based DED (IN718 DED). To achieve these objectives, this study compares the microstructure and mechanical properties of IN718 DED with and without the application of HF.

2. Materials and methods

2.1. Part printing

The present work used an in-house developed directed energy deposition (DED) 3D printer combined with *in situ* interlayer hot forging (HF-DED) prototype (Fig. 1), which consists of a gas metal arc welding machine power source (CITOWAVE III 520) assembled in a 3-axis CNC machine [40,46]. The HF system comprises a moving part (shielding gas nozzle) driven by two pneumatic actuators that move following a linear guideway/bearing system. The forging tool design was previously optimized (20 mm) [39], considering the forging temperature range of Ni-based superalloys (900–1100 °C) [51]. Single-bead multi-layer parts, $7 \times 30 \times 120$ mm^3, were fabricated (DED and HF-DED) using the deposition parameters summarized in Table 1. Table 2 depicts the feedstock material composition. A detailed description of the development of the deposition parameters can be found in the Supplementary Material.

2.2. Post-deposition heat treatment

Sequentially, the samples underwent the PDHT depicted in Fig. 2a. This heat treatment was previously developed for IN718 DED, considering a long soaking time to induce a notorious dissolution of the secondary phases and promote a high volume fraction of hardening phases (γ' and γ'' precipitates). For more details, refer to our previous work [8,9].

Table 1
– Inconel 718 fabricated by arc-based DED deposition parameters.

Arc-based DED	
Arc plasma current[a]	137 [A]
Arc plasma tension[a]	17 [V]
Wire feed speed	4 [m/min]
Travel speed	5 [mm/s]
Heat input[b]	373 [J/mm]
Interlayer temperature	150 [°C]
Contact-tip-to-work distance	12 [mm]
Shielding gas	I3-ArHe-25
Shielding gas specification	AWS A5.32
Shielding gas flow	15 [l/min]
Substrate preparation	ISO 8501-1
In situ interlayer hot forging	
Pneumatic pressure	5 [MPa]
Frequency	8 [Hz]

[a] Root mean square (RMS).
[b] Thermal efficiency ($\eta = 0.8$), BS EN 1011-1.

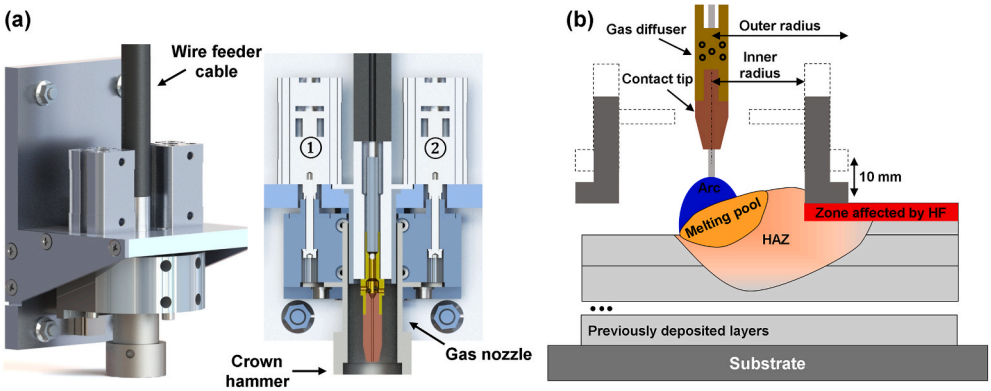

Fig. 1. – (a) *In situ* interlayer hot forging (HF) system and (b) schematic representation of the effect of HF during part printing. ① and ② are the pneumatic actuators.

Table 2
– Feedstock material (filler metal) chemical composition (% weight). Solid wire (ø 1.2 mm) supplied by voestalpine Böhler (3Dprint AM 718).

	Ni	Cr	Fe	Nb	Mo	Ti	Al	C	Mn	Si	P	S
Measured	52.52	17.41	20.23	5.25	2.98	0.98	0.45	0.05	0.04	0.08	0.002	0.001
AWS A5.14	50–55	17–21	Bal.	4.75–5.5	2.8–3.3	0.65–1.15	0.2–0.8	0.08	0.35	0.35	0.015	0.015
AMS 5383							0.4–0.8					
API 6ACRA				4.87–5.2		0.80–1.15	0.4–0.6	0.045	0.35	0.35	0.01	0.01

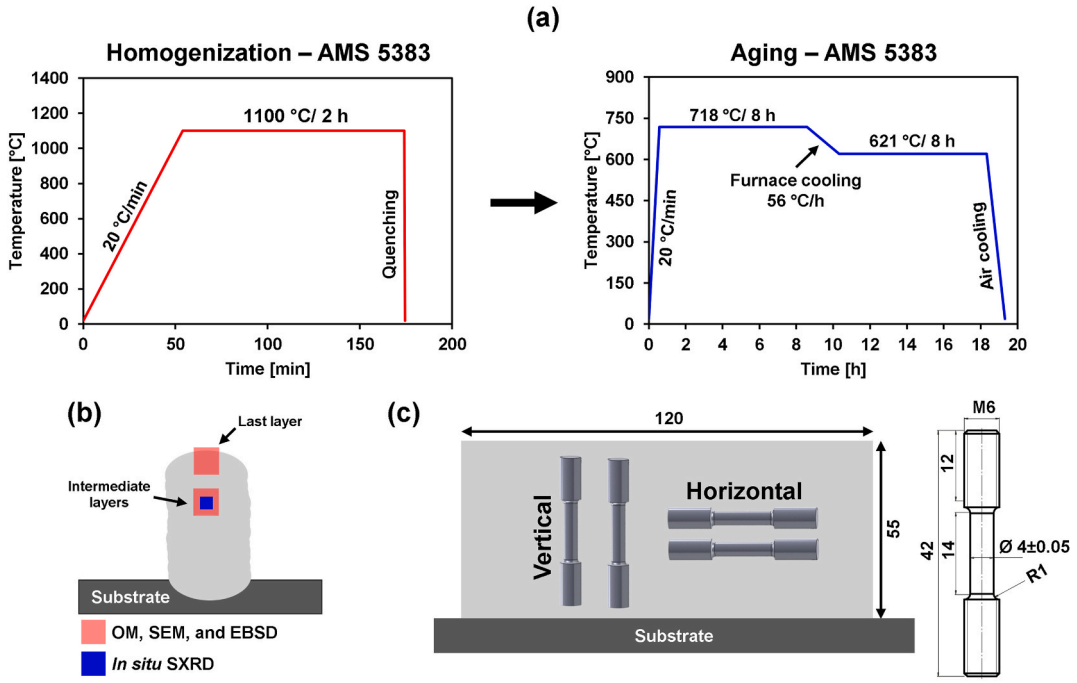

Fig. 2. – (a) Post-deposition heat treatment, (b) the position where the microstructure characterization analyses were conducted, and (c) the tensile test specimens and their orientation.

2.3. Microstructure characterization

Optical microscopy and electron scanning microscopy (SEM) samples were prepared using the metallographic method (ground and polished). The microstructure was revealed using electrolytic etching (10 wt% oxalic acid – $HO_2C{-}CO_2H$ – in water, 6 V for 25 s). Electron backscatter diffraction (EBSD) samples followed the same sequence, with an additional polishing step in a VibroMet® (SiO2, 0.04 μm, 6 h). SEM and EBSD analyses were conducted (Fig. 2b) using a field emission gun scanning electron microscope equipped with a high-velocity EBSD camera (EDAX® Velocity). The step size, voltage, and tilt angle used in EBSD analyses were 1 μm, 20 kV, and 70°, respectively. Data post-processing was performed using the MTEX-Toolbox [52].

In situ synchrotron X-ray diffraction (SXRD, PETRA III/DESY, Fig. 2c) was used to assess the microstructure evolution during the homogenization step of the PDHT (Fig. 2a). The analyses were performed in transmission mode with a wavelength of 0.14235 Å. Data post-processing (2D Debbye-Scherrer diffraction rings integration) was carried out using FIT2D [53] and an in-house developed Python-based routine [54]. For details on the experimental setup and data post-processing methodology, refer to our previous work [5].

2.4. Mechanical testing

2.4.1. Vickers microhardness

Vickers microhardness test was performed with a load of 0.3 kgf ($HV_{0.3}$) and a dwell time of 15 s. The procedure was conducted using a Mitutoyo HM-112 digital microhardness tester, following ISO 6507–1.

2.4.2. Tensile test at elevated-temperature (650 °C)

Tensile testing at 650 °C was performed to evaluate the effect of HF on the mechanical properties of IN718 DED. To the best of the author's knowledge, only two studies [2,19] have reported the elevated-temperature tensile behavior of IN718 DED (transferred plasma arc [2] and gas metal arc [19]). Furthermore, the cited works demonstrated inferior performance compared to the wrought material, highlighting a critical challenge for the industrial scalability of IN718 DED. This limitation is significant, especially considering the rigid AMS 5662 requirements for Inconel 718 used in the aviation industry (*e.g.*, turbine blades, discs, seals, rings, and casings).

Before the tensile tests, the specimens underwent a full PDHT (homogenization + aging, as shown in Fig. 2a). Tests were conducted using an Instron 8562 machine equipped with a 100 kN load cell, a contact extensometer, and a strain rate of $\sim 5.0{\cdot}10^{-4}$ s^{-1}. The specimens (Fig. 2c) were extracted along the building (vertical) and deposition (horizontal) directions. These specimens were machined from heat-treated printed parts using electric discharge machining, and their final dimensions were achieved through turning, followed by low-stress mechanical polishing of the gauge length zone. The data were analyzed and reported in accordance with the ASTM E8 and E21 standards. Furthermore, two specimens were evaluated for each condition.

3. Results

3.1. Effect of in situ interlayer hot forging on grain size

The IN718 DED showed (Fig. 3) the typical microstructure of Ni-

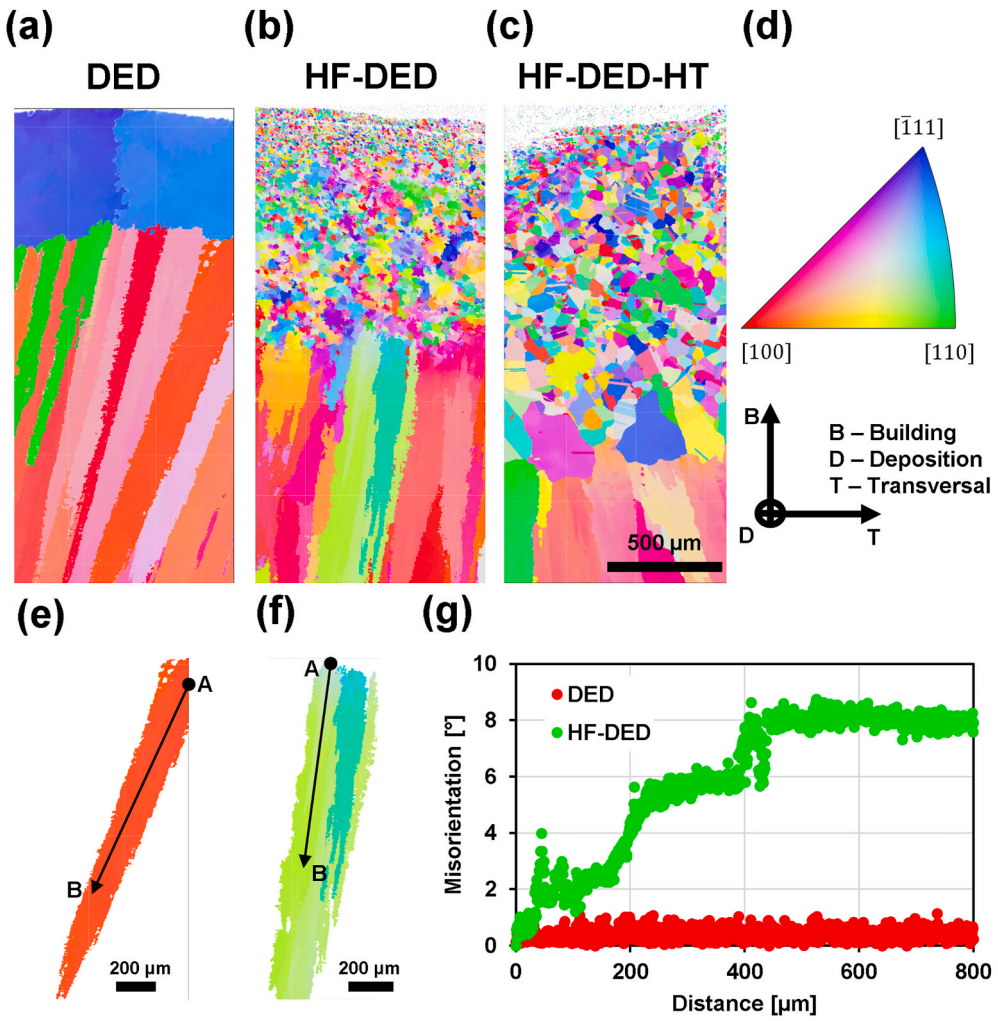

Fig. 3. – Comparison of the effect of interlayer hot forging on the microstructure of the top layer surface of Inconel 718 fabricated *via* arc-based DED: (a) without HF, (b) with HF, (c) with HF and HT, (d) the standard orientation triangle (color map) and sample orientation reference, (e) and (f) isolated grains located just posterior to the refined grain size zone in (a) and (b), respectively, and (g) intragranular misorientation from (e) and (f). Points A and B indicate the start and end points, respectively. The distance in (g) was normalized relative to the building direction. (For interpretation of the references to color in this figure legend, the reader is referred to the Web version of this article.)

based superalloys fabricated *via* arc-based DED [2–4,17–23,55], characterized by aligned and coarse columnar grains. Additionally, in the last moments of solidification (close to the top layer surface, Fig. 2b), a change in the solidification mode from columnar to equiaxial [10] is verified. According to Li et al. [12], as the solidification front advances (from the fusion line to the layer top surface), the reduction of the thermal gradient at the melting pool can promote the columnar-to-equiaxed transition [13]. However, Fig. 4a shows that the subsequently deposited layers (intermediate layer in Fig. 2b) completely remelted the columnar-to-equiaxed zone and promoted the epaxial grain growth, resulting in coarse columnar grains crossing several layers (millimetric-sized). Therefore, IN718 DED exhibits a non-optimized microstructure, failing to meet the material grain size requirements (Fig. 4c). Furthermore, it is worth noting that the coarse and oriented microstructure typically observed in IN718 DED persists even after prolonged soaking time and high peak temperature PDHT (Fig. 2a). In other words, adjusting the IN718 DED (gas metal arc) microstructure *via* PDHT is almost unfeasible.

The *in situ* interlayer hot forging (HF-DED) promoted the formation of a finer grain size zone on the top layer surface, which was larger than the columnar-to-equiaxed zone observed in conventionally fabricated DED parts (~0.5 vs. ~ 1 mm). This finer grain size zone is associated with a dynamic recrystallization effect induced by the imposed hot deformation [39]. Furthermore, after the heat treatment (HF-DED-HT), the refined grain size zone expands, attributed to post-dynamic recrystallization [57,58] and evidenced by the presence of multiple annealing twins (Fig. 1S, Supplementary Material). Therefore, the region that underwent deformation (storage energy) and did not experience dynamic recrystallization can subsequently recrystallize during the PDHT. This statement is corroborated by comparing the intragranular misorientation (Fig. 3) observed in the DED and HF-DED conditions for a columnar grain located immediately below the columnar-to-equiaxed transition region and the dynamically recrystallized grain region, respectively. DED exhibits the typical low intragranular misorientation of as-solidified materials (maximum misorientation of approximately 1°), which is associated with the solidification shrinkage and thermal deformation [59]. In contrast, HF-DED induced a pronounced intragranular misorientation that tends to stabilize as the depth in the sample increases, *i.e.*, HF induced an intragranular deformation gradient, as also previously reported for interlayer rolling and peening [43,60]. Additionally, the depth at which the misorientation stabilizes (~0.5 mm) and the length of the dynamically recrystallized zone (~1 mm) have a similar extension to the overall recrystallized zone after the PDHT (~1.5 mm).

HF-DED-HT exhibits intense static recrystallization, characterized by the majority (72 %) of grains with a shape factor lower than 3 (*i.e.*,

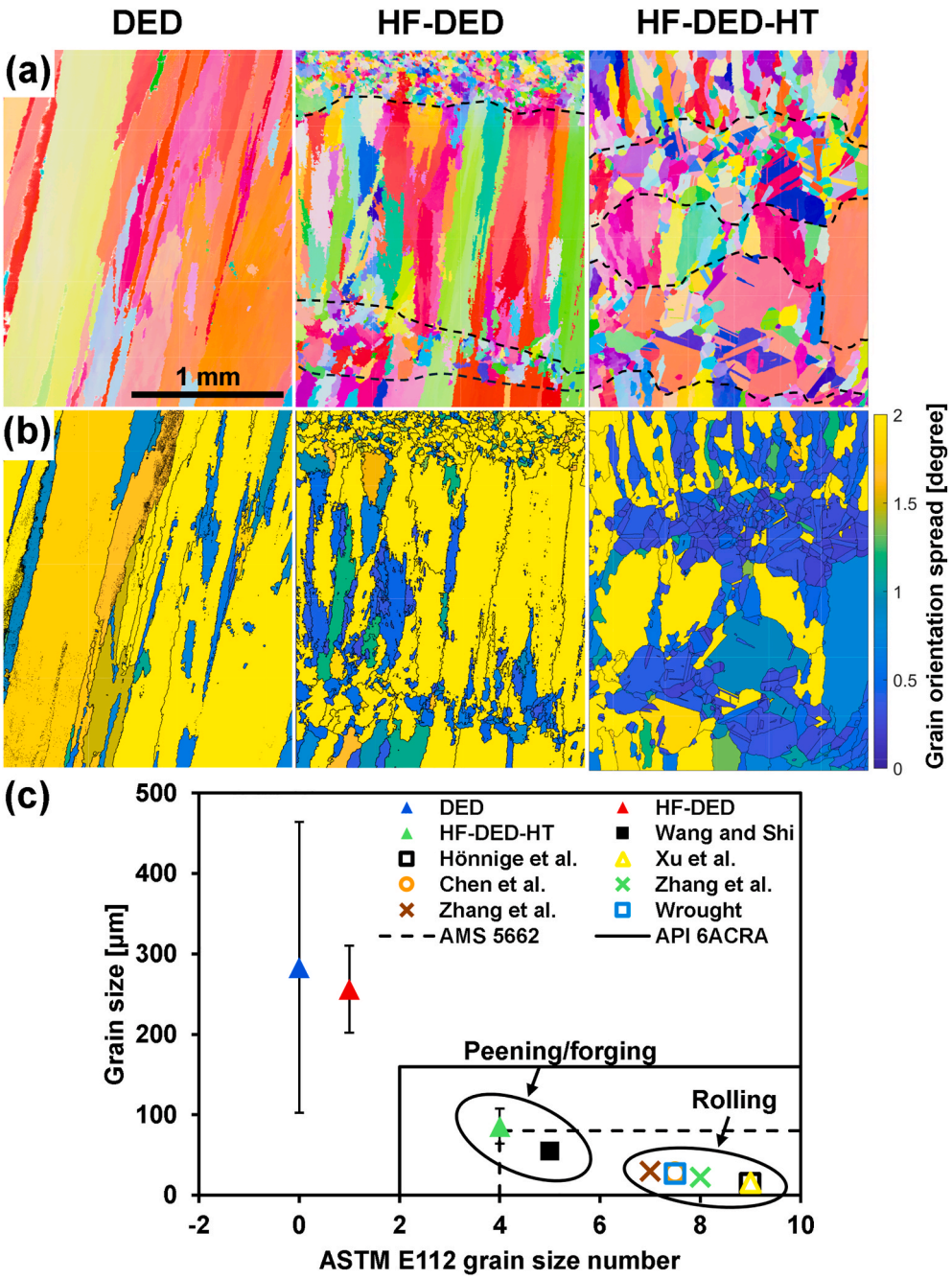

Fig. 4. – (a) Effect of interlayer hot forging on the microstructure of Inconel 718 fabricated *via* arc-based DED (color code and axis references are the same as in Fig. 3), (b) grain orientation spread distribution, and (c) the grain size measurement and its comparison with the literature. The EBSD analyses were performed at the printed part's central region, as indicated in Fig. 2b. The cited references are [20,42–44,47,56]. The dotted line in (a) for HF-DED represents the ribbon of recrystallized grains. (For interpretation of the references to color in this figure legend, the reader is referred to the Web version of this article.)

almost equiaxed microstructure, refer to Fig. 2S), lower GOS (<1°, Fig. 4b), and the presence of annealing twins (Fig. 4a). Moreover, as the size of the deformed zone (~1.5 mm) is smaller than the layer thickness (~2 mm), achieving a fully recrystallized microstructure is not feasible, leading to the presence of some columnar grains, *i.e.*, the portion of the deposited layer that undergoes plastic deformation will recrystallize, whereas the remaining portion (under elastic loading) will not. However, these columnar grains were partially consumed by the grain growth of the statically recrystallized grains. Furthermore, HF-DED-HT exhibited a finer microstructure than DED and HF-DED, meeting the material grain size requirements (Fig. 4c).

Fig. 4c compares the system (deposition unit + interlayer mechanical deformation) applied to DED processes (ASTM F3187), since they are not typically applied to powder bed fusion (PBF) processes due to the fast cooling rate (finer microstructure) and susceptibility to static recrystallization during post-deposition heat treatment (solving the coarse and oriented microstructure problem) [15,16]. Among the DED processes, as summarized by Farias et al. [33], hot interlayer deformation systems can be divided into rolling (quasi-static) and forging/peening (dynamic). The latter generally produces only a shallow deformation depth, which occurs due to two main aspects: (i) vibration induced by the impact, which demands robust equipment (robot arm or CNC machine); (ii) material fracture caused by localized and intense impact deformation. Therefore, due to the shallow deformation depth

and lower applied load (~3 kN [39] vs. 160 kN [67]), forging/peening systems typically achieve a lower grain size refinement effect compared to rolling. Consequently, HF exhibited a shallower deformed zone, leading to incomplete recrystallization of the deposited layer (Fig. 4), whereas interlayer rolling can induce static recrystallization throughout the part [47,48]. On the other hand, rolling systems limit deposition path planning, which contradicts the additive manufacturing philosophy of printing complex-shaped parts, restricting their application to linear parts (walls) or geometries with large curvature radii. HF possesses a greater flexibility and almost unrestricted path planning, which is associated with the co-axial crown hammer (Fig. 1). Regarding dynamic IDM systems, HF showed similar performance, as observed when comparing the present results with Hönnige et al. [45] (arc-based DED + cold peening) and Wang and Shi (laser-based DED + cold peening) [43]. These results further demonstrate the design success of HF and its ability to modify the microstructure of Inconel 718 parts fabricated *via* arc-based DED, without restricting path planning flexibility.

A highly oriented microstructure is another critical issue related to Ni-based alloys fabricated *via* arc-based DED, which can compromise material performance and induce highly anisotropic behavior [51,68,69]. The pole figures and 3D orientation distribution functions (Fig. 5) show that the IN718 DED exhibited a cube texture ({200}<100>), which is associated with the easy growth direction for face-centered cubic materials (<100>) and the epitaxial grain growth phenomenon [12–14]. HF-DED promoted some grain size refinement (Fig. 4a), which reduces its texture index compared to the DED counterpart. However, a cube texture aspect persists due to the presence of coarse columnar grains. The homogenization PDHT led to significant static recrystallization throughout the microstructure (Fig. 4), resulting in a non-oriented microstructure (Fig. 5). Therefore, HF can address two critical points related to additively manufactured Ni-based superalloys: (i) reducing the grain size through dynamic/static recrystallization and (ii) promoting a non-oriented microstructure.

From a materials processing perspective, as the IMD systems alter the microstructure of the deposited layers through their top surface, there is a clear relationship between grain size refinement efficiency and deposition parameters (the bead penetration). To significantly affect the microstructure, the penetration must be less than the IMD-affected zone (length equal to the stabilization of the intragranular misorientation).

3.2. Microstructure

3.2.1. As-built condition

Fig. 6 summarizes the as-built microstructure of Inconel 718 fabricated *via* arc plasma DED for conditions without (DED) and with *in situ* interlayer hot forging (HF-DED). IN718 DED showed columnar dendrites aligned with the building rection, which are in accordance with EBSD analysis (Fig. 4a). Otherwise, HF-DED presented a finer grain size with non-oriented dendrites, which was expressed by the non-aligned interdendritic precipitates. These results showed clear evidence of HF's effects on microstructure, supporting the EBSD analysis (Fig. 4b). Despite the HF effect on grain size, HF did not alter significantly the solidification conditions (solidification rate and thermal gradient) [46], which was supported by the similar secondary dendrite arm space (a function of cooling rate [70]) between DED and HF-DED (~12.99 vs. 12.93 μm, respectively). Thus, the interdendritic precipitates observed for DED and HF-DED tend to be similar since the cooling rate and alloy composition were not altered. Based on morphological and chemical aspects (Figs. 7 and 8), the interdendritic precipitates are distinguished in MC-type carbides and Laves phases. These analyses are also corroborated by the SXRD data and the Scheil-Gulliver solidification curve (Fig. 9). In addition, due to the needle-like aspect, δ phase was also identified (Fig. 7), which is related to the multiple thermal cycles observed during part printing [71]. The MC-type carbides, (Ti,Nb)C, showed a shell-core aspect, where a higher Ti content characterizes the core, while the shell showed a higher Nb content (Fig. 8), a similar morphology was previously reported for Nb-bearing Ni-based superalloys (additive manufacturing and welding) [72–74]. Furthermore, the observed secondary phases (Laves, MC-type carbides, and δ phase) for the as-built conditions (DED and HF-DED) followed the results obtained

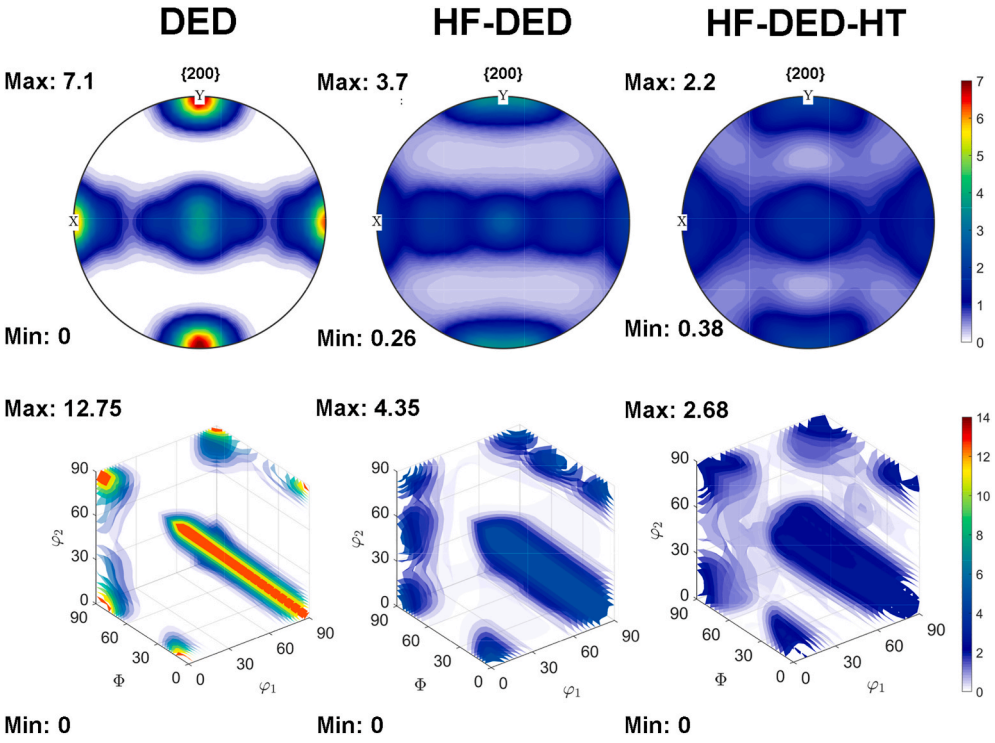

Fig. 5. – Comparison of the effect of *in situ* interlayer hot forging on the texture aspect of the Inconel 718 fabricated *via* arc-based DED. The pole figures and 3D orientation distribution functions were estimated using EBSD data (Fig. 4).

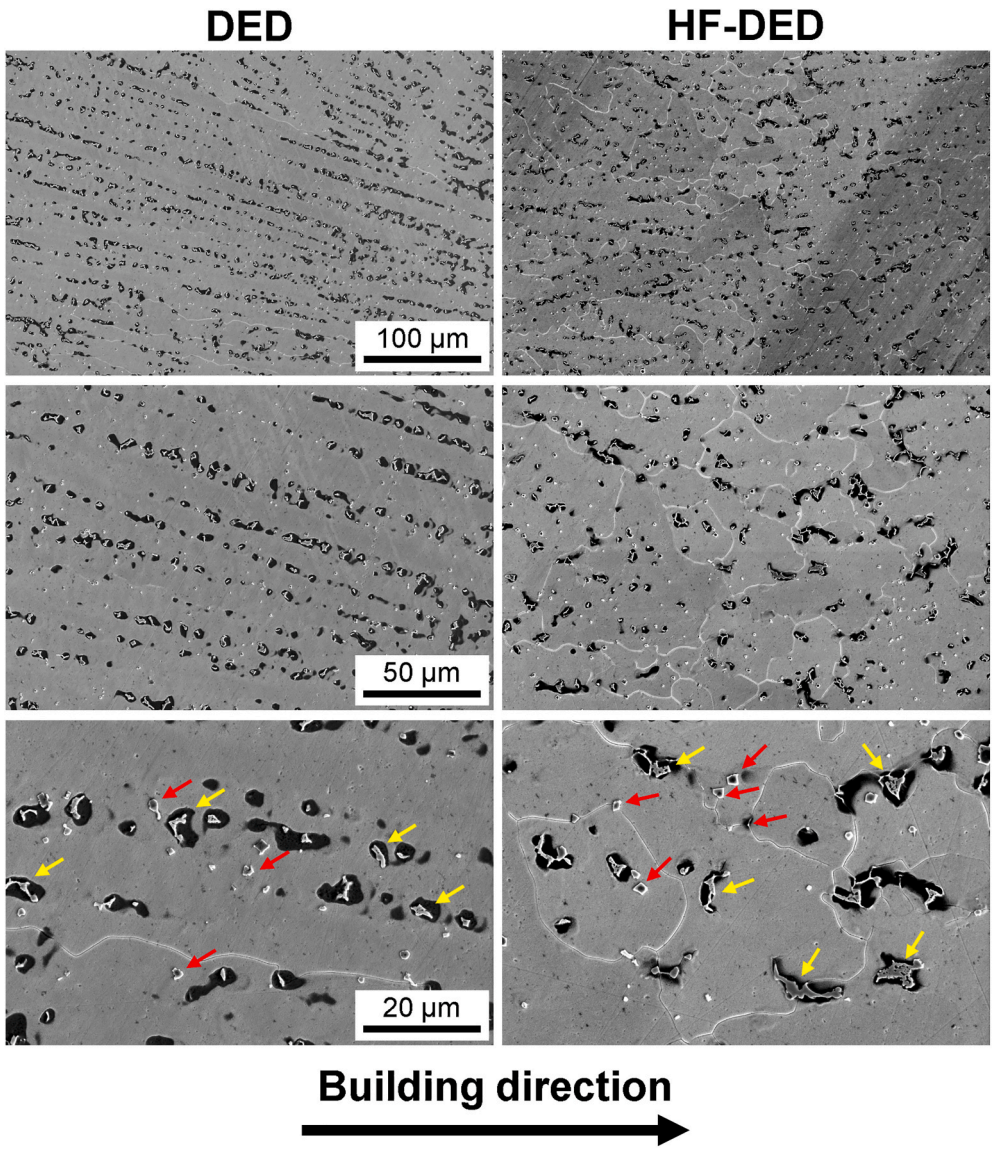

Fig. 6. – Microstructure of the Inconel 718 fabricated *via* arc plasma DED: condition without (DED) and with *in situ* interlayer hot forging (HF-DED). The red and yellow arrows indicate the MC-type carbides and Laves phase, respectively. (For interpretation of the references to color in this figure legend, the reader is referred to the Web version of this article.)

by Oh et al. [75] (*in situ* SXRD during laser-DED of IN718) and those predicted by the experimental solidification models (Knorovsky et al. [76] and DuPont et al. [77]). Therefore, based on scanning electron microscopy results, it is possible to indicate that the main effect of HF on the microstructure aspect of the IN718 DED was related to the grain size and dendrite orientation.

3.2.2. Heat-treated condition

After the homogenization step of the heat treatment schedule (Fig. 10), a significant difference in microstructure can be observed between DED and HF-DED, particularly in the grain size and grain morphology. The HF-DED condition resulted in an almost equiaxed grain structure, whereas the DED counterpart maintained a columnar and oriented grain structure. In addition, the long-chain Laves and δ phase typically observed in as-built condition (Fig. 7) had their morphology significantly altered (Laves – partial dissolution from long-chain to dotted aspect – and δ – total dissolution, Fig. 11). Furthermore, according to Ruan et al. [78], some primary MC-type carbides (yellow circles in Fig. 10) can pin the grain boundary migration (grain growth) during the heat treatment, which can contribute to controlling the final grain size for HF-DED (Fig. 4). The scanning electron microscopy results (Fig. 10) demonstrated that the IN718 DED (gas metal arc) grain size and stereology are almost insensitive to the PDHT. Otherwise, HF coupled with the PDHT induces significant changes in grain size and morphological aspects, promoting a fine and non-oriented microstructure.

3.3. Mechanical properties

3.3.1. Microhardness

The Vickers microhardness profile was measured to evaluate the effect of the *in situ* interlayer hot forging onthe mechanical behavior at room temperature of the Inconel 718 fabricated *via* arc plasma DED (Fig. 12a). For the as-built condition, HF-DED increased (~30 HV) the material hardness compared to DED. Moreover, it is possible to verify that the peaks and valleys in the microhardness profile of HF-DED and DED are out of phase (minimum of HF-DED equaling the maximum of DED), which evidences the remaining deformation (dislocation density strengthening) and corroborates the misorientation profile (Fig. 3).

During part printing (DED condition), regions near the fusion line exhibit finer dendrites (higher cooling rate), which coarsen as the

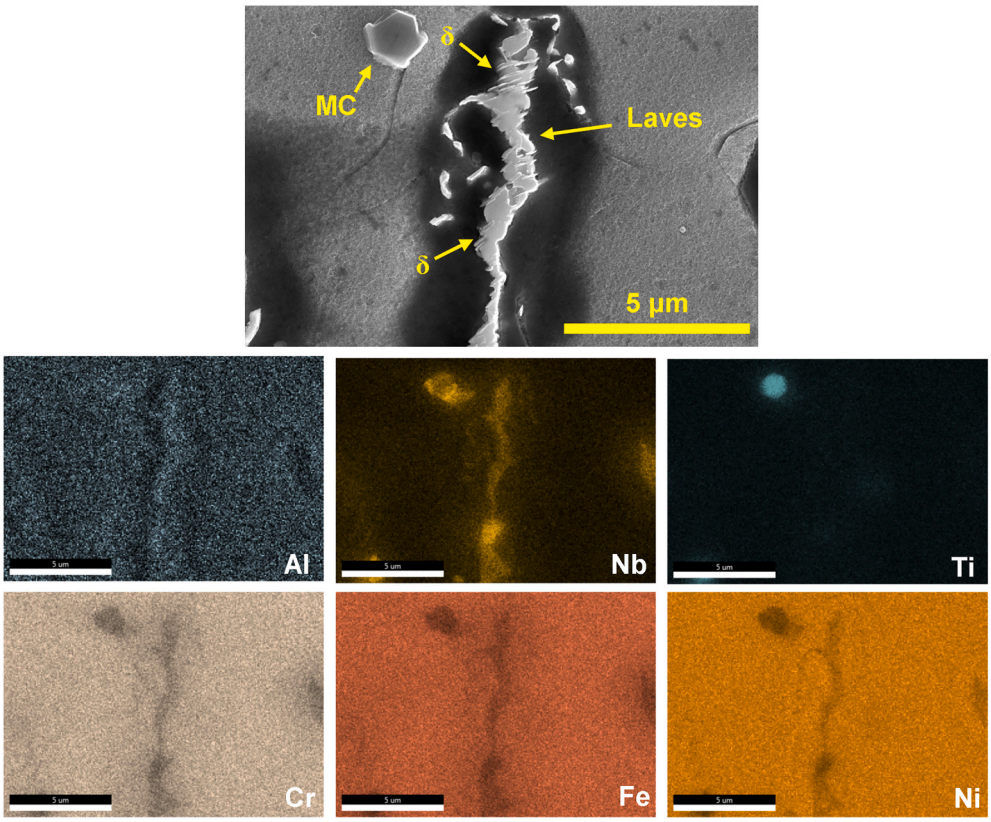

Fig. 7. – Scanning electron microscopy and Energy-dispersive X-ray spectroscopy of the interdendritic region.

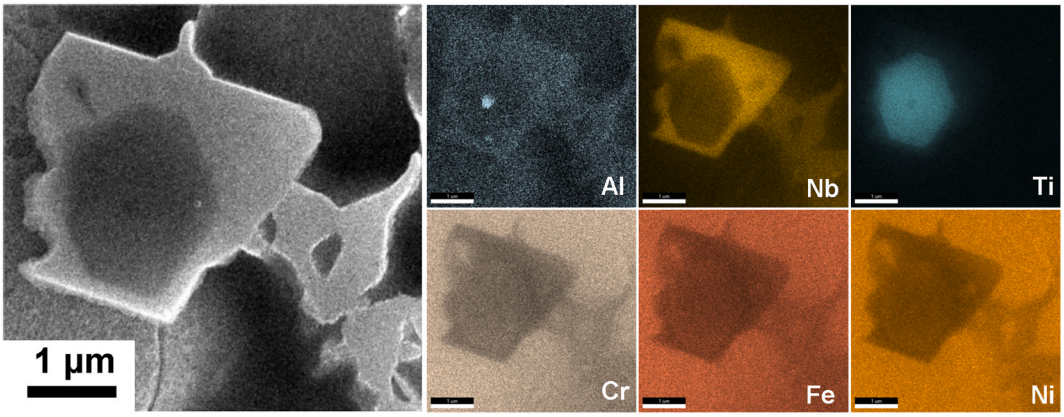

Fig. 8. – High magnificence scanning electron microscopy and Energy-dispersive X-ray spectroscopy on interdendritic precipitate.

solidification front progresses [79]. In practical terms (refer to schematic representation in Fig. 13), if hardness indentation occurs close to the fusion line, it is expected to be higher (finer microstructure) compared to measurements taken near the top layer surface (coarse microstructure). Thus, hardness peaks and valleys occur throughout the hardness profile due to distinct 'hard' and 'soft' regions in each layer. In contrast, for the HF-DED condition, the 'soft' region corresponds to the area near the fusion line, unaffected by mechanical deformation (fine dendrites and misorientation stabilization, Fig. 4), while the deformed region (top layer surface) becomes harder (dislocation density strengthening). As a result, an out-of-phase pattern emerges in the hardness. As previously demonstrated (Fig. 4), the remaining deformation, namely, the intragranular misorientation (Fig. 3), which is macroscopically expressed as an increase in hardness, serves as the driving force for static recrystallization during the heat treatment (homogenization step).

In relation to heat-treated conditions (Fig. 12b), no significant difference was observed between DED and HF-DED. This result was expected, as the grain boundary (Hall-Petch relation) and dislocation density (Bailey-Hirsh's relation) strengthening have the least hardening contribution for Inconel 718 at the heat-treated state (precipitation-strengthened alloy), as previously computed by Farias et al. [8,9] (1100 °C/2 h + aging), Zhang et al. [80] (1150 °C/1.5 h + aging), and Sui et al. [81] (1040 °C/45 min + aging) for additively manufactured IN718. Compared to the available literature (Fig. 12c), the present work exhibited similar hardness to wrought and PBF materials and met the AMS 5662 hardness requirement (331 Brinell hardness, converted to 346 HV using ASTM E140). When comparing the present results to those reported for IN718 DED (different heat treatment conditions), a higher hardness was observed, reinforcing the validity of the designed PDHT

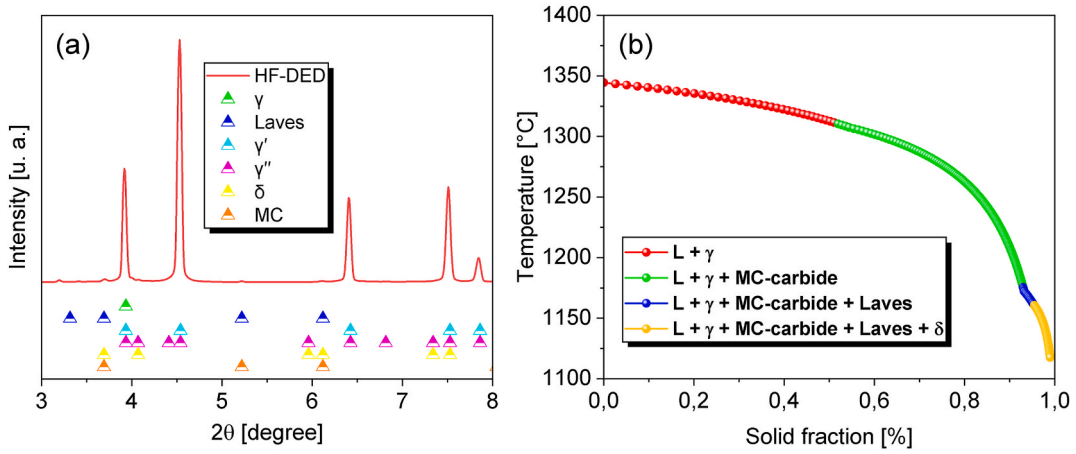

Fig. 9. – (a) Synchrotron X-ray diffraction and (b) Schiel-Gulliver solidification model (Thermo-calc® and TCNI12 database) of the Inconel 718 fabricated *via* arc plasma DED.

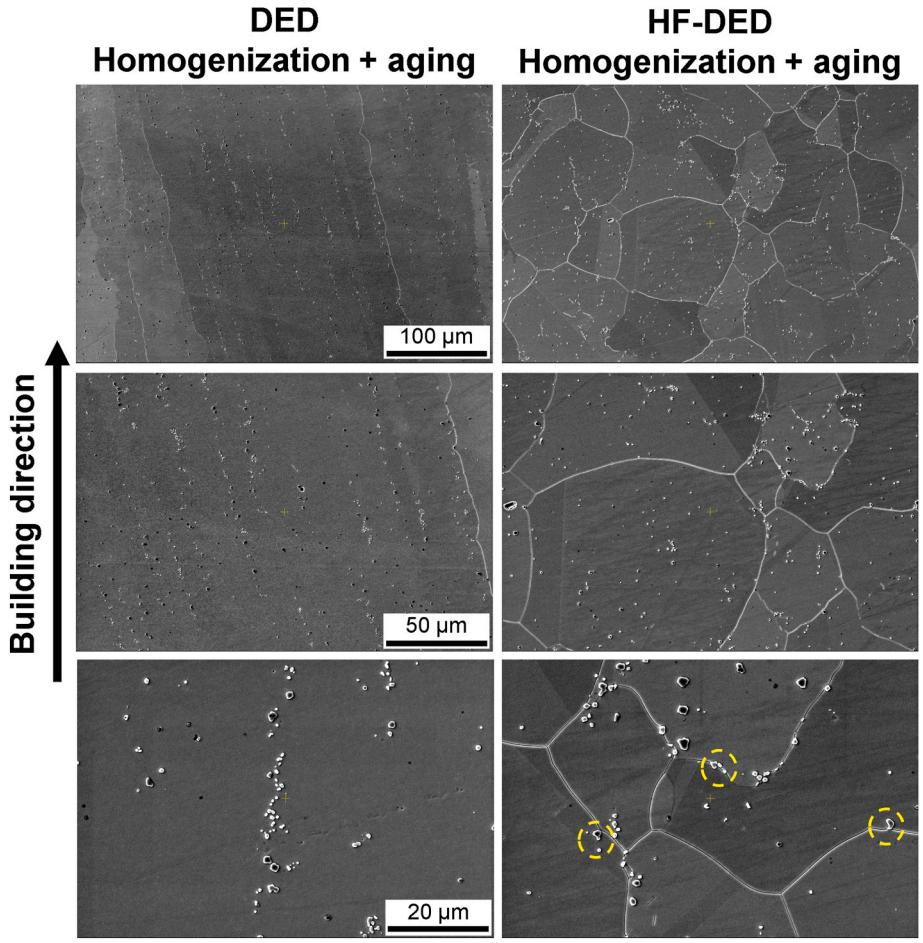

Fig. 10. – Effect of post-deposition heat treatment (1100 °C/2 h + aging) on the microstructure of Inconel 718 fabricated *via* DED and HF-DED.

[9]. Furthermore, compared to Zhang et al. [19] (450 HV) and Xu et al. [42] (443 HV), who also employed interlayer mechanical deformation (warm and cold rolling, respectively), the present results exhibit a similar magnitude (Fig. 12c). These findings emphasize the effectiveness of HF in altering the non-optimized microstructure of the IN718 DED and enhancing the material's performance.

3.3.2. *Elevated-temperature tensile testing*

Fig. 14 depicts the elevated-temperature tensile testing results, where both conditions (DED and HF-DED) exhibited the typical strain-stress curve characteristic of ductile materials, meeting the elongation requirements specified in AMS 5662. Additionally, IN718 DED accomplished the yield strength (*YS*) requirement (AMS 5662) for the vertical direction, while IN718 HF-DED was able to meet the *YS* requirements for both directions (vertical and horizontal). To the best of the authors'

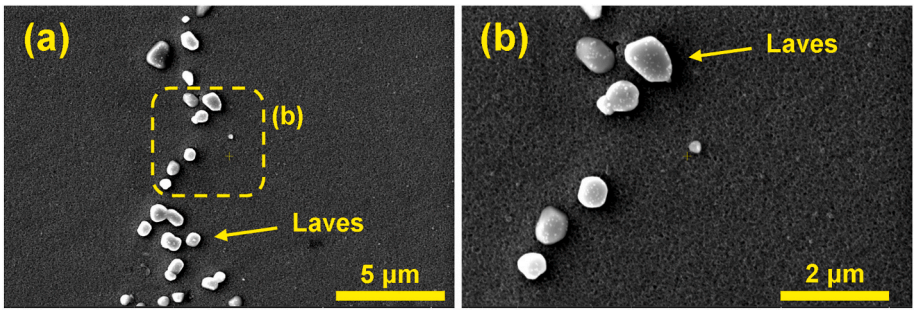

Fig. 11. – (a) and (b) Partial dissolution of Laves phases due to post-deposition heat treatment. The Laves phase in as-built condition (Fig. 9) exhibited a long-chain aspect. After post-deposition heat treatment, it is partially dissolved.

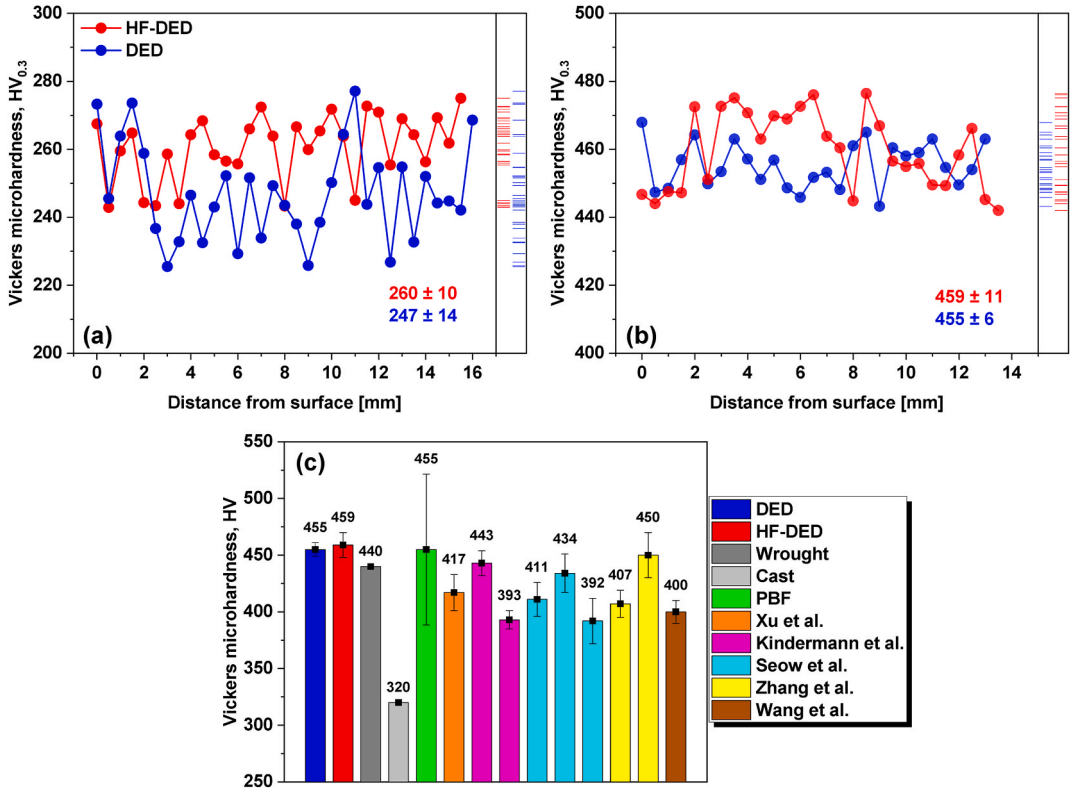

Fig. 12. – Vicker microhardness profile ($HV_{0.3}$) of the Inconel 718 fabricated *via* arc plasma DED with and without Interlayer hot forging: (a) as-built, (b) heat-treated, and (c) comparison with the literature data. The cited works are, in sequence, wrought, cast, and PBF [82], Xu et al. [42], Kindermann et al. [3], Seow et al. [2], Zhang et al. [19], Wang et al. [83].

knowledge, this is the first report of IN718 DED simultaneously meeting the elongation and *YS* requirements at elevated-temperature. Previously, Zhang et al. [19] (IN718 DED + interlayer warm rolling) demonstrated that the strength requirements could be met at the expense of ductility. Additionally, HF-DED exhibited an almost isotropic *YS*, which was primarily associated with its non-oriented microstructure and almost equiaxed grains (Fig. 5).

Comparing the present results with those reported in the literature, the present results (particularly HF-DED) demonstrate improvements in relation to Seow et al. [2] (plasma transferred arc DED) and Zhang et al. [19] (gas metal arc DED). Seow et al. [2], using a higher temperature heat treatment (1186 °C/0.66 h + aging), promoted undesirable secondary grain growth, jeopardizing the material's performance. Otherwise, Zhang et al. [19] used a lower solution heat treatment temperature (970 °C/1 h + aging), promoting insufficient Laves dissolution and the δ-phase precipitation, resulting in low elongation and *YS*. In relation to laser-based AM processes (laser-DED [84] and laser-PBF [86]) with higher temperature heat treatments (1050 °C/0.75 h + aging and 1093 °C/1 h + aging, respectively), the HF-DED shows inferior performance. This behavior is expected since laser-based PBF exhibited a finer grain size than DED and HF-DED, as well as the fast cooling rate induces a finer solidification microstructure (cellular vs. coarse dendrites) and segregation pattern, which produces homogeneous chemical composition (after heat treatment) and hardening phases distribution. However, for low temperature heat-treated PBF (980 °C/1 h + aging), the HF-DED and DED results were equivalent to laser-PBF [87] and electron beam PBF [85]. It is important to note that PBF and DED, although both AM processes, belong to different classes. Therefore, a direct comparison is intended only to provide a general perspective on the mechanical properties at elevated-temperatures and on the improvements induced by HF-DED, rather than to compare different classes of AM processes directly.

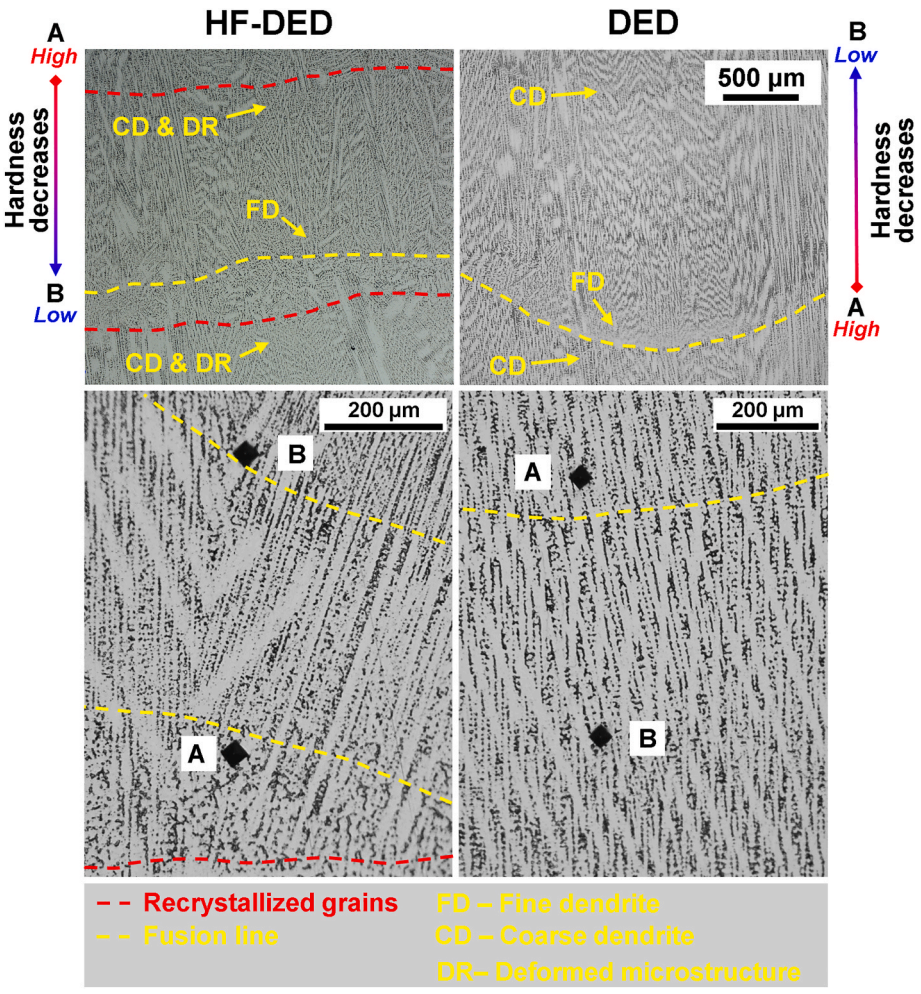

Fig. 13. – Correlation between the microstructure and hardness profile of Inconel 718 fabricated *via* DED and HF-DED at as-built condition.

4. Discussion

4.1. Grain size refinement mechanism

Considering that Inconel 718 is a low/medium stacking fault energy alloy, among the restoration phenomena (*e.g.*, recovery and recrystallization), recrystallization is favored due to the large separation between partial Shockley dislocations [61]. This makes dislocation constriction, cross-slip, annihilation, and cell formation (recovery) more difficult. On the other hand, it promotes high-angle grain boundary migration (recrystallization), as evidenced by the change in grain size and shape on the top layer surface (EBSD data, Fig. 3). In addition, the rapid deformation (deformation stroke at a strain rate of 300 s^{-1} [46]) results in a high Zener–Hollomon parameter, which also favor dynamic recrystallization over recovery. Therefore, despite the complex correlation between thermal aspects (cooling cycles) and the deformation gradient, where both cooling rate and deformation rate decrease as distance increase from top layer surface and fusion line, it can be inferred from the abovementioned evidence (stacking fault energy, grain size, and morphology) that the main restoration mechanism active during *in situ* interlayer hot forging was recrystallization (dynamic and static).

In relation to static recrystallization (post-deposition heat treatment), the deformation gradient (dislocation density), evidenced by the misorientation gradient (Fig. 3g), influences the static nucleation rate and consequently the grain size. Regions with higher misorientation (*i.e.*, higher dislocation density) exhibit a faster nucleation rate [62]. Consequently, regions close to the fusion zone, which present higher misorientation, tend to develop a finer grain size due to the larger number of nuclei formed. In contrast, regions farther from the fusion zone tend to exhibit a coarser grain size, as clearly demonstrated in Fig. 3c and 4a.

Analyzing the effect of the subsequently deposited layers on the HF-DED (Fig. 4a), it is possible to observe a small ribbon of recrystallized grains (dotted black lines), which are almost equiaxed and have a grain spread orientation (GOS, Fig. 4b) less than 1° [63]. These recrystallized grains either remained (*i.e.*, did not melt) from the previously deposited layer (dynamically recrystallized) or recrystallized during the multiple reheating thermal cycles. The differentiation between them can be evidenced by the presence of columnar grains with similar orientation both before and after the ribbon of recrystallized grains. Thus, these new grains did not participate in the subsequent deposited layer solidification and were nucleated during the multiple reheating thermal cycles (refer to the schematic representation – Fig. 15). Additionally, away from the layer's center, a distinct orientation is observed before and after the ribbon of recrystallized grains, *i.e.*, these grains persist (not totally remelted) after the subsequent layer deposition, acting as an almost non-oriented substrate. The presence or absence of remaining dynamically recrystallized grains can be directly correlated with the finger-type penetration aspect of gas metal arc-based DED (Fig. 15) [64]. Thus, the region far away from the layer center (non-completely remelted) tends to have a finer microstructure than in the layer center, as reported by Gao et al. [65] (arc-based DED + interlayer incremental forming). The grain size refinement mechanism observed for IN718 HF-DED closely resembles that reported by Wang and Shi [43] (Inconel

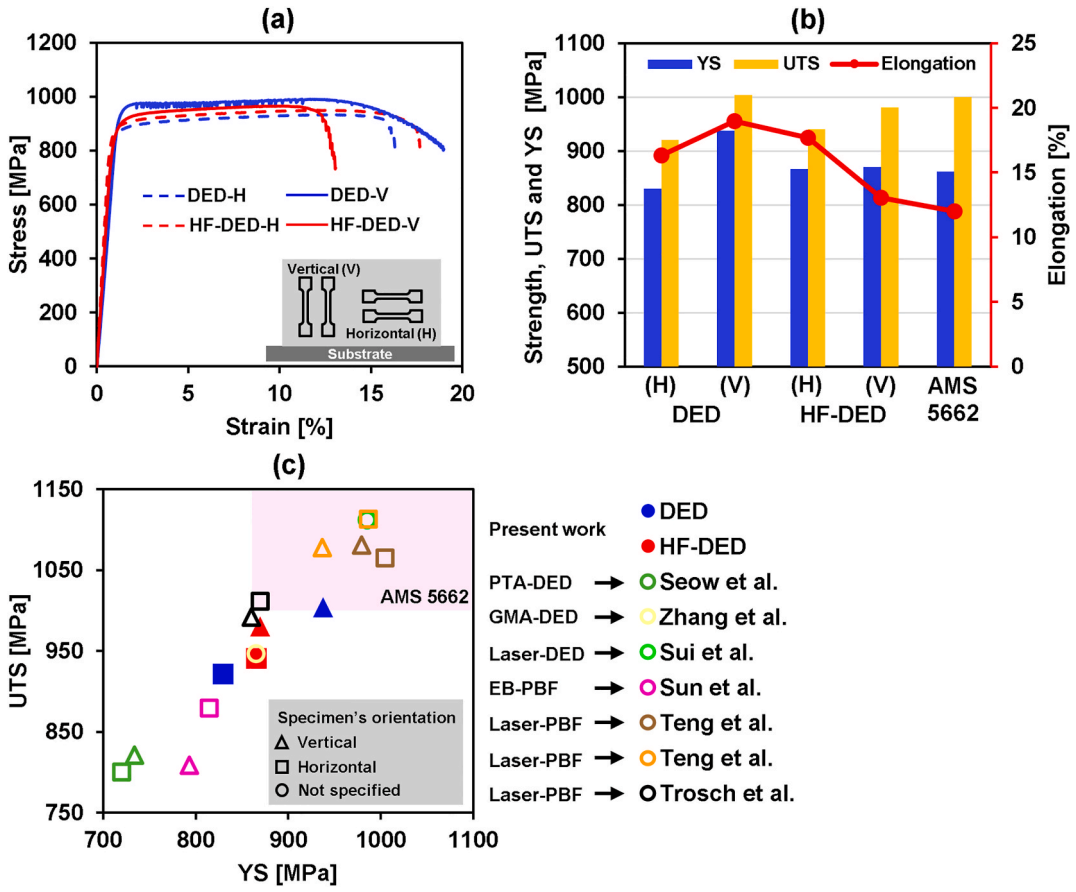

Fig. 14. – Elevated-temperature (650 °C) tensile test of the Inconel 718 fabricated *via* arc plasma DED: (a) tensile-strain curve, (b) tensile properties results, and (c) comparison with the literature. The references cited are Seow et al. [2], Zhang et al. [19], Sui et al. [84], Sun et al. [85], Teng et al. [86], and Trosch et al. [87].

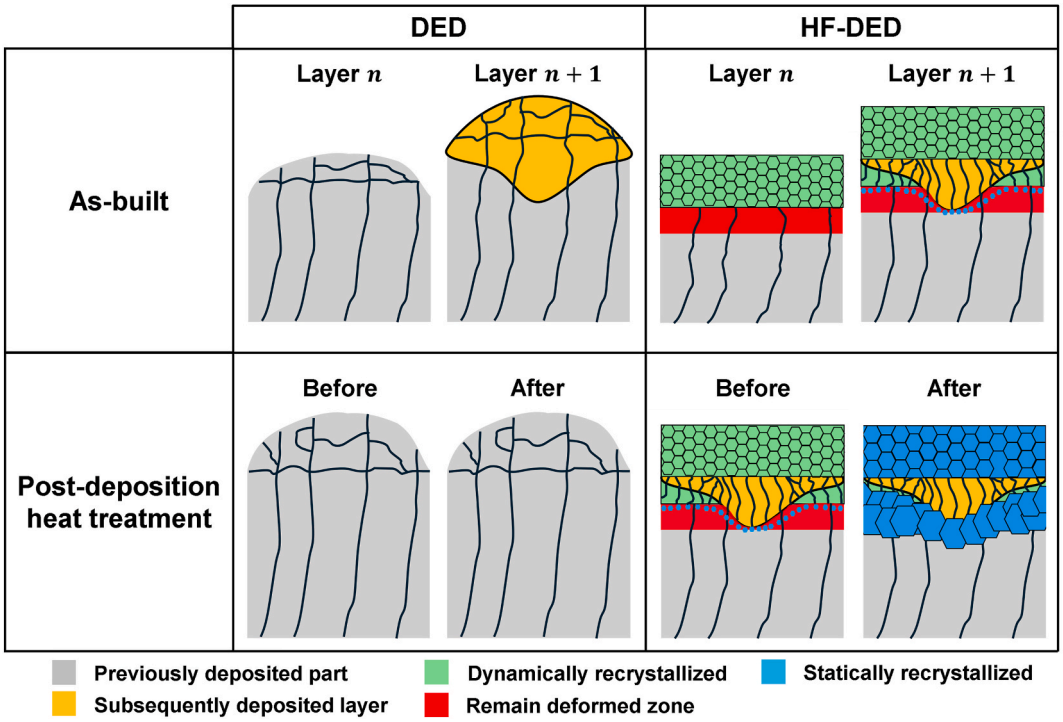

Fig. 15. – Schematic representation of the grain size refinement of the *in situ* interlayer hot forging for alloys that did not undergo allotropic solid-state phase transformation.

718 laser-DED + interlayer cold ultrasonic peening). However, it differs in that the deformed zone is incompletely melted due to the lower penetration of laser-DED compared to arc-based DED. Furthermore, it is worth mentioning that the columnar grain width in the HF-DED was lower than that of the DED, which can be attributed to the melting pool vibration induced by the hot forging strokes (dynamic loading) and the consequent restriction of lateral growth during solidification [40,50,66].

In situ SXRD (Fig. 16) reveals that the IN718 DED experienced non-significant changes during PDHT (also reported by EBSD data, Fig. 3S), as evidenced by the smooth alterations in the 2D Debye-Scherrer diffraction rings (Fig. 16b) and full width at half maximum (FWHM, Fig. 16c). Moreover, it is noteworthy that 2D Debye-Scherrer diffraction rings exhibited a dotted pattern [14], which serves as volumetric evidence of the coarse microstructure of IN718 DED. These results are also corroborated by tracking the {200} diffraction peak intensity (Fig. 16c), *i.e.*, the grain size and texture aspects of IN718 DED are almost insensitive to PDHT, which is consistent with existing literature [2–4,8,17–24,55] and EBSD data (Fig. 3S, Supplementary Material). HF-DED showed a notable decrease in FWHM during PDHT

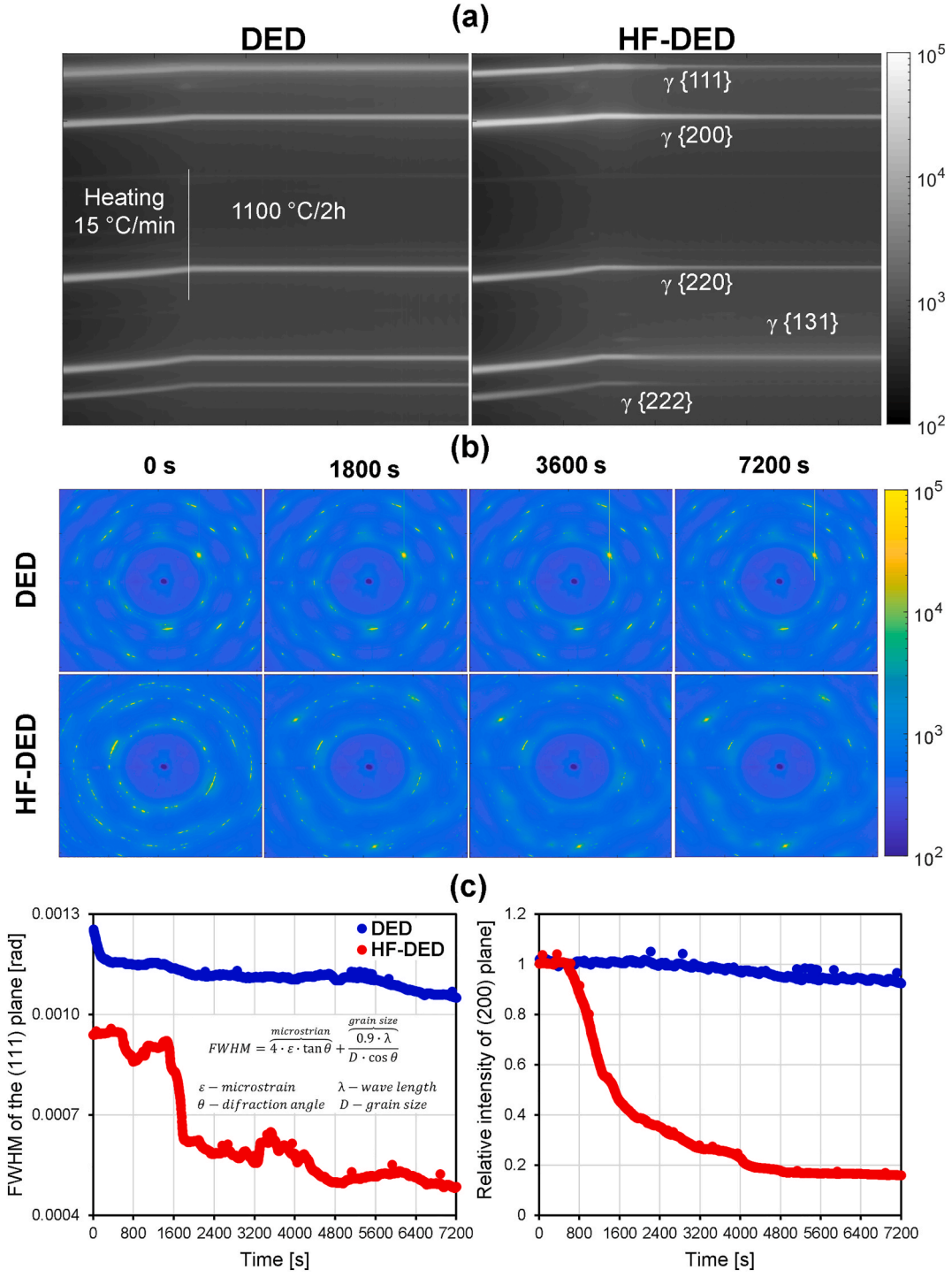

Fig. 16. – *In situ* synchrotron X-ray diffraction data. (a) The diffractograms evolution with the time, (b) examples of 2D Debye-Scherrer diffraction rings alteration with the time, and (c) full width at half maximum (FWHM) and peak intensity evolution of the {111} and {200} diffraction peaks, respectively.

(Fig. 16c), which is linked to restoration phenomena (recovery and recrystallization) [61]. Moreover, for medium/low stacking fault energy materials (*e.g.*, Inconel 718) [88], the main restoration phenomena are typically attributed to recrystallization, as evidenced by Fig. 4. At approximately 1500 s (Fig. 16c), an intense reduction in FWHM is observed, which was correlated with a decrease in microstrain due to recrystallization [89–91]. Subsequently (3200–4000 s), the slight increase in FWHM is associated with an increase in grain number; finally (4000–7200 s), the slight reduction in FWHM can be related to grain growth (both a reduction in microstrain and grain number). In addition, the intensity of the {200} diffraction peak continually decreased for HF-DED, indicating that static recrystallization and grain growth substantially modified the primary microstructure during PDHT. *In situ* SXRD results support the previously presented *ex situ* evidence (Figs. 3 and 4) used to describe the grain size refinement mechanism induced by *in situ* interlayer hot forging.

4.2. Elevated-temperature tensile behavior

The strengthening mechanisms observed in Inconel 718, particularly those associated with age hardening (γ' and γ'' precipitates), are dependent on loading orientation and crystallographic texture [81,92–96], which can be rationalized by the Taylor factor [97]. Cube texturized materials (such as IN718 DED, Fig. 5) exhibited a lower Taylor factor [9, 98] compared to non-oriented materials [9], which is also observed in the present work when comparing DED and HF-DED (Fig. 4S – Supplementary Material). Farias *et al.* [8], Liang et al. [99], and Sazerat et al. [100] demonstrated that, due to the columnar grain structures typically observed in additively manufactured Ni-based superalloys, the plane transverse to the building direction exhibits a less oriented microstructure (higher Taylor factor) compared to the plane parallel to the building direction. Consequently, the horizontal specimens (cross-section parallel to the building direction) tend to have lower strength than the vertical specimens due to the softer nature of the cube-textured material (lower Taylor factor) [2,9,97]. In addition to crystallographic aspects, at elevated-temperatures, the grain cores become stronger than the grain boundary regions [101], where deformation tends to concentrate. This means that a larger grain boundary area can reduce the material's performance at elevated-temperatures, especially the elongation and consequently the ultimate tensile strength – *UTS*. Therefore, HF-DED can have dual effects: (i) refining the grain size and inducing a non-oriented microstructure (*i.e.*, strengthening the material) and (ii) increasing the grain boundary length (*i.e.*, reducing material performance) [101].

In the DED condition, since the horizontal specimens are perpendicular to the columnar grains (refer to Fig. 17), plastic deformation tends to initiate and concentrate at the grain boundaries, resulting in lower elongation than the vertical specimens, which in consequence resulted in a lower *UTS*. In the vertical specimens, both the grain core and grain boundaries underwent the same loading (an iso-stress state), which leads to a homogeneous deformation in both regions and a consequent increase in the elongation and *UTS*. Therefore, the observed anisotropic behavior for DED (elongation, *YS*, and *UTS*) and the superior performance of vertical specimens can be explained based on the crystallographic texture (Taylor factor, *i.e.*, *YS* and *UTS*) and grain stereology (columnar grains, *i.e.*, elongation and *UTS*). Unlike DED, the HF-DED induced an almost non-oriented microstructure (Fig. 5), characterized by a banded structure composed of recrystallized grains and remaining primary columnar grains (Figs. 3 and 4). Thus, due to the formation of the ribbon of the recrystallized grains (Fig. 4), vertical specimens experienced heterogeneous elastic strain, as Young's modulus depends on crystallographic orientation [102]. This tends to concentrate deformation in regions with a lower Young's modulus (remaining primary grains, refer to Fig. 17), inducing a lower *YS* compared to DED. Additionally, the higher grain boundary density (finer grain size) reduces ductility and, consequently, lowers the *UTS* of vertical specimens compared to conventional DED. Regarding horizontal specimens, HF-DED enhances elongation, *YS*, and *UTS* compared to DED. The improvement in material's performance can be directly associated with the finer and less oriented microstructure (Figs. 4 and 5), which enhances material strength (strengthening mechanisms depend on crystallographic texture [81,92–96]) and reduces deformation concentration in the remaining columnar grains (*i.e.*, deformation is most homogeneous). Therefore, HF-DED was able to simultaneously eliminate the *YS* anisotropy and induce a material strength similar to that observed for the Inconel 718 fabricated by several additive manufacturing processes (*e.g.*, DED and PBF), while also meeting the AMS 5662 elongation requirement.

The fractography of horizontal specimens (Fig. 18) revealed a clear ductile fracture mode aspect (DED and HF-DED), reinforcing the observed tensile-strain curves and the higher elongation (Fig. 14). DED conditions showed the typical fractography of Ni-based superalloys fabricated by fusion-based additive manufacturing and welding [2,4,19, 26,44,84], where the dimples tends to nucleate in the incoherent interface between the Laves phase and the matrix (γ), creating the 'solidification' (dendritic) pattern aspect on the fracture surface (refer to yellow arrows in Fig. 18). On the other hand, the grain size refinement and non-aligned Laves phase (Fig. 7) induced by HF-DED altered the fracture surface, resulting in a mix of oriented and non-oriented dimple patterns (primary columnar and recrystallized grains, respectively). About the vertical specimens, no significant difference was observed between the DED and HF-DED (Fig. 5S, Supplementary Material), both of which exhibited a ductile fracture aspect (nucleation and coalescence of microvoids, presumably from remaining undissolved Laves particles).

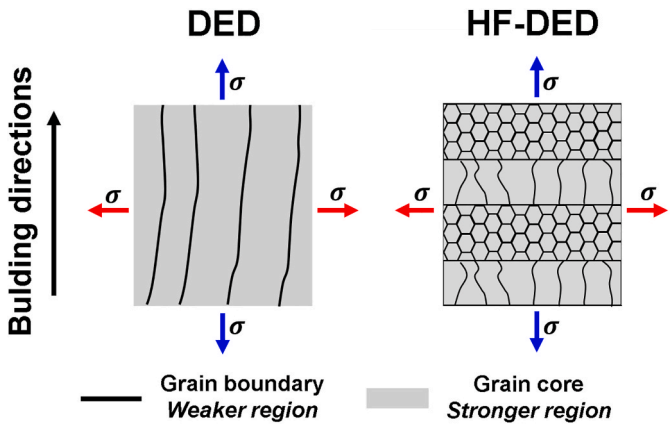

Fig. 17. – Schematic representation of the loading direction and the microstructure aspects.

4.3. Considerations and practical implications of in situ interlayer hot forging

As previously reported [33], the introduction of interlayer mechanical deformation makes the DED system more complex and costly, which can put the HF-DED industrial use and scalability into question, especially due to it does not deliver significant gains in overall mechanical properties. However, considering the HF-DED's capacity to induce an isotropic material, the cost-performance trade-off may justified in specific scenarios, especially for applications in structural components subjected to multi-axial loading, complex stress states (structural service condition), or cyclic loading [103,104]. In addition, another potential application of HF-DED is in repair operations. Farias et al. [105] summarized that, although DED has often been considered suitable for repair, its coarse microstructure can result in a 'softer' repaired region compared with the harder base material. This issue is particularly critical for age-hardened alloys (*e.g.*, Inconel 718), where high-temperature heat treatments (dissolve interdendritic eutectics) cannot be applied

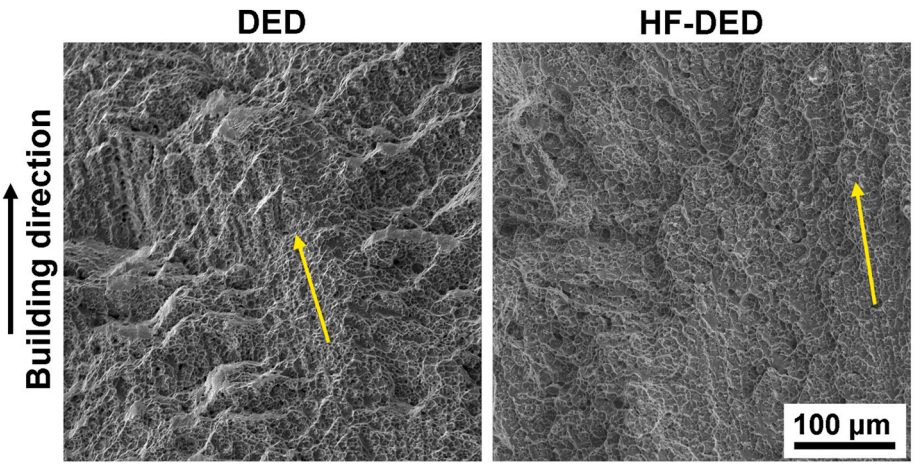

Fig. 18. – Fractography of horizontal specimens tensile tested at 650 °C. The yellow arrow indicates the 'solidification' dimples pattern. The fractography of vertical specimens is shown in Fig. 5S (Supplementary Material). (For interpretation of the references to color in this figure legend, the reader is referred to the Web version of this article.)

without compromising the integrity of the base material [106]. Another interesting application of HF-DED lies in its ability to tune the microstructure locally. By alternating between HF-DED and conventional DED, it is possible to generate regions with finer, non-oriented grains alongside regions with coarser, oriented grains. The capability to locally tune the microstructure cannot be achieved solely by controlling deposition parameters in non-transformable alloys, due to the high penetration and broad thermal distribution characteristic of arc-based DED processes.

As demonstrated along the present work, HF-DED is able to significantly alter the grain size, grain morphology, and crystallography texture of IN718 DED (Figs. 3–5) through the combined effect of remaining deformation (induced by HF) and static recrystallization (post-deposition heat treatment), which eliminates the materials properties dependent on loading direction and allows to IN718 DED to meet the grain size requirements (AMS 5662). In other words, HF-DED promotes a finer grain size material with isotropic tensile properties (Fig. 14). Additionally, when comparing HF-DED and DED in a performance perspective, the HF-DED (horizontal direction) improves the strength properties (especially YS and UTS) in relation to DED; otherwise, for vertical direction, strength properties were slightly reduced, which is attributed to the generation of a duplex microstructure (fine grains and remaining primary grains, Fig. 17). However, it is worth mentioning that the IN718 DED did not meet the YS requirement (AMS 5662) for both directions, which is only achieved through the HF-DED, even when compared with the previous literature (Fig. 14c).

One critical point to highlight in relation to HF-DED is the correlation between the deformation depth (dynamic recrystallized zone + deformed zone), penetration, and layer thickness. As represented in Fig. 15, if the penetration is deeper than the deformation induced by HF, its entire effect will be erased. Thus, HF restricts the DED process window, where low penetration parameters are recommended. Otherwise, when the penetration is inferior to the deformation depth, the remaining deformation zone (*i.e.*, that which was not fully remelted) will undergo a double grain size refinement (deposition of subsequent layers and post-deposition heat treatment). However, this refined grain region is smaller than the original layer thickness, where remnant and partially recrystallized columnar grains persist. Thus, considering the dynamic aspect of the HF and its limitation in inducing high depth deformation without a layer malformation, promoting a fully recrystallized layer becomes a challenge. In relation to thick parts (multi-layer multi-bead), Duarte [107] demonstrates that HF-DED can print them without inducing geometry and path planning limitations.

Therefore, the use of HF-DED can be justified by its ability to promote a fine and non-oriented microstructure, resulting in isotropic tensile behavior. These aspects are particularly important for Ni-based superalloys (*e.g.*, Inconel 718), which typically exhibit a coarse and oriented microstructure and are used in critical conditions (*e.g.*, stringent material requirements). In this regard, *in situ* interlayer hot forging emerges as an alternative to improve the microstructural aspects of non-transformable alloys [105]. However, in applications where the combination of adequate performance and a refined microstructure does not justify the increased system complexity and production costs, the use of HF-DED is not advisable.

5. Conclusions

The present work evaluated the effect of the *in situ* interlayer hot forging (HF) on the microstructure and mechanical properties at elevated-temperatures of the Inconel 718 fabricated by arc-based directed energy deposition (DED). The grain size refinement mechanism of HF-DED was carefully described. The first mechanism is attributed to the dynamically recrystallized zone generated by localized deformation at the top surface of the just-deposited layer. This localized deformation also induces a non-recrystallized zone (remaining deformation), which can subsequently experience recrystallization during reheating thermal cycles and/or post-deposition heat treatments. This significantly altered the grain size (from columnar to equiaxed, meeting the AMS 5662 requirement) and crystallographic texture (from cube texture to almost non-oriented). Furthermore, IN718 HF-DED exhibited almost isotropic behavior during the elevated-temperature tensile test and met the elongation and yield strength requirements of AMS 5662. These results underscore the effectiveness of dynamic interlayer deformation systems in refining grain size and improving the performance of parts fabricated *via* arc-based DED.

CRediT authorship contribution statement

Francisco Werley Cipriano Farias: Writing – original draft, Validation, Methodology, Investigation, Formal analysis, Data curation, Conceptualization. **Valdemar Rebelo Duarte:** Writing – original draft, Investigation, Formal analysis, Conceptualization. **João da Cruz Payão Filho:** Validation, Software. **Norbert Schell:** Resources, Investigation. **Emad Maawad:** Investigation. **Jonathan Cormier:** Writing – review & editing, Methodology, Investigation. **Fabio Machado Alves da Fonseca:** Methodology, Investigation. **Antonio J. Ramirez:** Resources, Methodology, Investigation. **Telmo Jorge Gomes dos Santos:** Writing – review & editing, Supervision, Resources, Project administration,

Investigation, Funding acquisition, Formal analysis, Data curation, Conceptualization. **J.P. Oliveira:** Writing – review & editing, Visualization, Supervision, Resources, Project administration, Methodology, Investigation, Funding acquisition, Formal analysis, Data curation, Conceptualization.

Disclaimer

One of the authors of this article is part of the Editorial Board of the journal. To avoid potential conflicts of interest, the responsibility for the editorial and peer review process of this article lies with the journal's other editors. Furthermore, the authors of this article were removed from the peer review process and had no, and will not have any access to confidential information related to the editorial process of this article.

Declaration of competing interest

The authors declare that they have no known competing financial interests or personal relationships that could have appeared to influence the work reported in this paper.

Acknowledgments

Authors acknowledge the Portuguese Fundação para a Ciência e a Tecnologia (FCT – MCTES) for its financial support *via* the project UID/EMS/00667/2019 (UNIDEMI). JPO acknowledges funding by national funds from FCT - Fundação para a Ciência e a Tecnologia, I.P., in the scope of the projects LA/P/0037/2020, UIDP/50025/2020 and UIDB/50025/2020 of the Associate Laboratory Institute of Nanostructures, Nanomodelling and Nanofabrication – i3N. Funding of CENIMAT/i3N by national funds through the FCT-Fundação para a Ciência e a Tecnologia, I.P., within the scope of Multiannual Financing of R&D Units, reference UIDB/50025/2020–2023 is also acknowledge. FWCF acknowledges Fundação para a Ciência e a Tecnologia (FCT-MCTES) for funding the Ph. D. Grant 2022.13870.BD. The authors acknowledge DESY (Hamburg, Germany), a member of the Helmholtz Association HGF, for the provision of experimental facilities. Beamtime was allocated for proposal I-20210986 EC. The research leading to this result has been supported by the project CALIPSOplus under the Grant Agreement 730872 from the EU Framework Programme for Research and Innovation HORIZON 2020. This activity has received funding from the European Institute of Innovation and Technology (EIT) Raw Materials through the project Smart WAAM: Microstructural Engineering and Integrated Non-Destructive Testing. FWCF acknowledges The Manufacturing and Materials Joining Innovation Center (MA^2JIC) and the Center for Electron Microscopy and Analysis (CEMAS) for the available facilities used during the development of this work. Institut Pprime gratefully acknowledges "Contrat de Plan Etat - Région Nouvelle-Aquitaine (CPER)" as well as the "Fonds Européen de Développement Régional (FEDER)" for their financial support to part of the reported work.

Appendix A. Supplementary data

Supplementary data to this article can be found online at https://doi.org/10.1016/j.msea.2025.149269.

Data availability

Data will be made available on request.

References

[1] M.N. de S. Lira, J. da Cruz Payão Filho, R.R. Nogueira, F.W.C. Farias, From CAD to part certification: 2.5%Cr–1%Mo steel flange fabricated via arc-based directed energy deposition, Prog. Addit. Manuf. (2025), https://doi.org/10.1007/s40964-025-01242-x.

[2] C.E. Seow, H.E. Coules, G. Wu, R.H.U. Khan, X. Xu, S. Williams, Wire + Arc Additively manufactured inconel 718: effect of post-deposition heat treatments on microstructure and tensile properties, Mater. Des. 183 (2019) 108157, https://doi.org/10.1016/j.matdes.2019.108157.

[3] R.M. Kindermann, M.J. Roy, R. Morana, P.B. Prangnell, Process response of inconel 718 to wire + arc additive manufacturing with cold metal transfer, Mater. Des. 195 (2020) 109031, https://doi.org/10.1016/j.matdes.2020.109031.

[4] R.M.M. Kindermann, M.J.J. Roy, R. Morana, J.A.A. Francis, Effects of microstructural heterogeneity and structural defects on the mechanical behaviour of wire + arc additively manufactured inconel 718 components, Mater. Sci. Eng. 839 (2022) 142826, https://doi.org/10.1016/j.msea.2022.142826.

[5] F.W.C. Farias, V.R. Duarte, I.O. Felice, J. da C.P. Filho, N. Schell, E. Maawad, J. Y. Li, Y. Zhang, T.G. Santos, J.P. Oliveira, In situ interlayer hot forging arc plasma directed energy deposition of inconel® 625: microstructure evolution during heat treatments, J. Alloys Compd. 952 (2023) 170059, https://doi.org/10.1016/j.jallcom.2023.170059.

[6] J. Nakrani, N.K. Mishra, V. Ajay, W. Yan, A. Shrivastava, Viability of WAAM for fabrication/repair of SS316: fatigue crack growth behavior for varied notch locations in the vicinity of WAAM-substrate interface, Theor. Appl. Fract. Mech. 133 (2024) 104527, https://doi.org/10.1016/j.tafmec.2024.104527.

[7] A. Rahimi, M. Yazdizadeh, M.V. Ara, M. Pouranvari, Strength and ductility of additively manufactured 310 austenitic stainless steel via wire-arc directed energy deposition: the role of columnar grain growth and ductility-dip cracking, Mater. Sci. Eng. 920 (2025) 147554, https://doi.org/10.1016/j.msea.2024.147554.

[8] F.W.C. Farias, V.R. Duarte, J. da Cruz Payão Filho, A.R. Figueiredo, N. Schell, E. Maawad, F.M. Alves da Fonseca, J. Cormier, A.J. Ramirez, T.G. Santos, J. P. Oliveira, Ni-based superalloy 718 fabricated by arc-based directed energy deposition: an experimentally-based strengthening mechanisms analysis, Mater. Sci. Eng. 939 (2025) 148417, https://doi.org/10.1016/j.msea.2025.148417.

[9] F.W.C. Farias, V.R. Duarte, J. da C.P. Payão Filho, A.R. Figueiredo, N. Schell, E. Maawad, J.Y. Li, Y. Zhang, M. Bordas-Czaplicki, F.M.A. da Fonseca, J. Cormier, T.G. Santos, J.P. Oliveira, High-performance Ni-based superalloy 718 fabricated via arc plasma directed energy deposition: effect of post-deposition heat treatments on microstructure and mechanical properties, Addit. Manuf. 88 (2024) 104252, https://doi.org/10.1016/j.addma.2024.104252.

[10] M. Gustafsson, M. Thuvander, E.L. Bergqvist, E. Keehan, L. Karlsson, Effect of welding procedure on texture and strength of nickel based weld metal, Sci. Technol. Weld. Join. 12 (2013) 549–555, https://doi.org/10.1179/174329307X213800.

[11] M. Gäumann, S. Henry, F. Cléton, J.D. Wagnière, W. Kurz, Epitaxial laser metal forming: analysis of microstructure formation, Mater. Sci. Eng. 271 (1999) 232–241, https://doi.org/10.1016/S0921-5093(99)00202-6.

[12] S. Li, J.Y. Li, Z.W. Jiang, Y. Cheng, Y.Z. Li, S. Tang, J.Z. Leng, H.X. Chen, Y. Zou, Y.H. Zhao, J.P. Oliveira, Y. Zhang, K.H. Wang, Controlling the columnar-to-equiaxed transition during directed energy deposition of inconel 625, Addit. Manuf. 57 (2022) 102958, https://doi.org/10.1016/j.addma.2022.102958.

[13] M. Gäumann, C. Bezençon, P. Canalis, W. Kurz, Single-crystal laser deposition of superalloys: processing–microstructure maps, Acta Mater. 49 (2001) 1051–1062, https://doi.org/10.1016/S1359-6454(00)00367-0.

[14] F. Schmeiser, E. Krohmer, C. Wagner, N. Schell, E. Uhlmann, W. Reimers, In situ microstructure analysis of inconel 625 during laser powder bed fusion, J. Mater. Sci. 57 (2021) 9663–9677, https://doi.org/10.1007/s10853-021-06577-8.

[15] S. Götelid, T. Ma, C. Lyphout, J. Vang, E. Stålnacke, J. Holmberg, S. Hosseini, A. Strondl, Effect of post-processing on microstructure and mechanical properties of alloy 718 fabricated using powder bed fusion additive manufacturing processes, Rapid Prototyp. J. 27 (2021) 1617–1632, https://doi.org/10.1108/RPJ-12-2019-0310.

[16] S. Taller, T. Austin, Using post-processing heat treatments to elucidate precipitate strengthening of additively manufactured superalloy 718, Addit. Manuf. 60 (2022) 103280, https://doi.org/10.1016/j.addma.2022.103280.

[17] N. Xi, X. Fang, Y. Duan, Q. Zhang, K. Huang, Wire arc additive manufacturing of inconel 718: constitutive modelling and its microstructure basis, J. Manuf. Process. 75 (2022) 1134–1143, https://doi.org/10.1016/j.jmapro.2022.01.067.

[18] N. Xi, K. Tang, X. Fang, Y. Li, Y. Duan, K. Huang, Enhanced comprehensive properties of directed energy deposited inconel 718 by a novel integrated deposition strategy, J. Mater. Sci. Technol. 141 (2023) 42–55, https://doi.org/10.1016/j.jmst.2022.09.026.

[19] T. Zhang, H. Li, H. Gong, Y. Wu, A.S. Ahmad, X. Chen, Effect of rolling force on tensile properties of additively manufactured inconel 718 at ambient and elevated temperatures, J. Alloys Compd. 884 (2021) 161050, https://doi.org/10.1016/j.jallcom.2021.161050.

[20] T. Zhang, H. Li, H. Gong, J. Ding, Y. Wu, C. Diao, X. Zhang, S. Williams, Hybrid wire - arc additive manufacture and effect of rolling process on microstructure and tensile properties of inconel 718, J. Mater. Process. Technol. 299 (2022) 117361, https://doi.org/10.1016/j.jmatprotec.2021.117361.

[21] T. Zhang, H. Li, H. Gong, Y. Wu, A.S. Ahmad, X. Chen, X. Zhang, Comparative analysis of cold and warm rolling on tensile properties and microstructure of additive manufactured inconel 718, Arch. Civ. Mech. Eng. 22 (2022) 1–14, https://doi.org/10.1007/s43452-021-00356-7.

[22] T. Zhang, H. Li, H. Gong, Y. Wu, X. Chen, X. Zhang, Study on location-related thermal cycles and microstructure variation of additively manufactured inconel 718, J. Mater. Res. Technol. 18 (2022) 3056–3072, https://doi.org/10.1016/j.jmrt.2022.03.178.

[23] T. Bhujangrao, F. Veiga, A. Suárez, E. Iriondo, F.G. Mata, High-temperature mechanical properties of IN718 alloy: Comparison of additive manufactured and

wrought samples, Crystals 10 (2020) 1–13, https://doi.org/10.3390/cryst10080689.
[24] F.W.C. Farias, V.R. Duarte, J. da C. Payão Filho, N. Schell, E. Maawad, M. Bordas-Czaplicki, F.M.A. da Fonseca, J. Cormier, T.J.G. dos Santos, J.P. Oliveira, Arc-based directed energy deposited inconel 718: role of heat treatments on high-temperature tensile behavior, Mater. Res. Lett. 12 (2024) 97–107, https://doi.org/10.1080/21663831.2023.2297734.
[25] D. Clark, M.R. Bache, M.T. Whittaker, Shaped metal deposition of a nickel alloy for aero engine applications, J. Mater. Process. Technol. 203 (2008) 439–448, https://doi.org/10.1016/J.JMATPROTEC.2007.10.051.
[26] C.E. Seow, J. Zhang, H.E. Coules, G. Wu, C. Jones, J. Ding, S. Williams, Effect of crack-like defects on the fracture behaviour of Wire + Arc Additively manufactured nickel-base alloy 718, Addit. Manuf. 36 (2020) 101578, https://doi.org/10.1016/j.addma.2020.101578.
[27] W.S. James, S. Ganguly, G. Pardal, Selection and performance of AM superalloys for high-speed flight environments, Int. J. Adv. Manuf. Technol. 122 (2022) 1–9, https://doi.org/10.1007/S00170-022-10005-9.
[28] J. Guzman, K.C. Riffel, W. Evans, E. Brizes, N. Avedissian, F.W.C. Farias, A. J. Ramirez, Weldability study of alloys 625 and 718 fabricated by laser-based additive manufacturing, J. Manuf. Process. 141 (2025) 556–569, https://doi.org/10.1016/j.jmapro.2025.02.051.
[29] T.A. Rodrigues, V.R. Duarte, D. Tomás, J.A. Avila, J.D. Escobar, E. Rossinyol, N. Schell, T.G. Santos, J.P. Oliveira, In-situ strengthening of a high strength low alloy steel during wire and arc additive manufacturing (WAAM), Addit. Manuf. 34 (2020) 101200, https://doi.org/10.1016/j.addma.2020.101200.
[30] T.A. Rodrigues, A. Malfeito, F.W.C. Farias, V. Duarte, J. Lopes, J. da Cruz Payão Filho, J.A. Avila, N. Schell, T.G. Santos, J.P. Oliveira, Grain refinement of inconel 625 during wire-based directed energy deposition additive manufacturing by in-situ added TiB2 particles: process development, microstructure evolution and mechanical characterization, Intermetallics 175 (2024) 108540, https://doi.org/10.1016/j.intermet.2024.108540.
[31] I.-T. Ho, D. Tiparti, Z. Liu, S. Tin, Insight to potential of TiB 2 and CeO 2 inoculants on microstructural evolution in laser powder bed fusion processed superalloy IN718, Metall. Mater. Trans. 55 (2024) 261–277, https://doi.org/10.1007/s11661-023-07247-x.
[32] L. Jia, H. Yi, F. Jiao, H. Cao, Particle floating and transfer effect in cored wire arc additive manufacturing: formation mechanism and laser shock inhibition, Int. J. Mach. Tool Manufact. 207 (2025) 104260, https://doi.org/10.1016/j.ijmachtools.2025.104260.
[33] F.W.C. Farias, T.J.G. dos Santos, J.P. Oliveira, Directed energy deposition + mechanical interlayer deformation additive manufacturing: a state-of-the-art literature review, Int. J. Adv. Manuf. Technol. 131 (2024) 999–1038, https://doi.org/10.1007/s00170-024-13126-5.
[34] P.A. Colegrove, J. Donoghue, F. Martina, J. Gu, P. Prangnell, J. Hönnige, Application of bulk deformation methods for microstructural and material property improvement and residual stress and distortion control in additively manufactured components, Scr. Mater. 135 (2017) 111–118, https://doi.org/10.1016/j.scriptamat.2016.10.031.
[35] B.S. Cota, D.A.E. Amendoeira, F.W.C. Farias, P.P. Fonseca, J.P. Oliveira, A. M. Moreno-Uribe, V.F. Viebranz, T. Hassel, T.G. Santos, V.R. Duarte, High-strength low-alloy steel fabricated by in situ interlayer hot forging arc-based directed energy deposition assisted with direct cooling: microstructural and mechanical properties evaluation, J. Manuf. Process. 129 (2024) 273–291, https://doi.org/10.1016/j.jmapro.2024.08.064.
[36] P.P. Fonseca, V.R. Duarte, F.W.C. Farias, B.S. Cota, T. Silva, T.G. Santos, C. M. Machado, Enhancing manufacturing and post-processing properties of WAAM ER110 HSLA steel: in situ hot forging + post-deposited heat treatment effects on surface quality and specific cutting energy, Prog. Addit. Manuf. (2024), https://doi.org/10.1007/s40964-024-00814-7.
[37] F.W.C. Farias, J. da C. Payão Filho, V.H.P. Moraes e Oliveira, Prediction of the interpass temperature of a wire arc additive manufactured wall: FEM simulations and artificial neural network, Addit. Manuf. 48 (2021) 102387, https://doi.org/10.1016/j.addma.2021.102387.
[38] J. Jang, Y. Shin, J. Lee, S.H. Lee, Precipitation behavior and grain growth of inconel 718 deposited by induction heating-assisted laser directed energy deposition, Addit. Manuf. 100 (2025) 104678, https://doi.org/10.1016/j.addma.2025.104678.
[39] F.W.C. Farias, V.R. Duarte, I.O. Felice, J. da C.P. Filho, N. Schell, E. Maawad, J. A. Avila, J.Y. Li, Y. Zhang, T.G. Santos, J.P. Oliveira, In situ interlayer hot forging arc-based directed energy deposition of inconel® 625: process development and microstructure effects, Addit. Manuf. 66 (2023) 103476, https://doi.org/10.1016/j.addma.2023.103476.
[40] V.R. Duarte, T.A. Rodrigues, N. Schell, R.M. Miranda, J.P. Oliveira, T.G. Santos, Hot forging wire and arc additive manufacturing (HF-WAAM), Addit. Manuf. 35 (2020) 101193, https://doi.org/10.1016/j.addma.2020.101193.
[41] F. Martina, M.J. Roy, B.A. Szost, S. Terzi, P.A. Colegrove, S.W. Williams, P. J. Withers, J. Meyer, M. Hofmann, Residual stress of as-deposited and rolled wire +arc additive manufacturing Ti–6Al–4V components, Mater. Sci. Technol. 32 (2016) 1439–1448, https://doi.org/10.1080/02670836.2016.1142704.
[42] X. Xu, S. Ganguly, J. Ding, C.E. Seow, S. Williams, Enhancing mechanical properties of wire + arc additively manufactured INCONEL 718 superalloy through in-process thermomechanical processing, Mater. Des. 160 (2018) 1042–1051, https://doi.org/10.1016/j.matdes.2018.10.038.
[43] Y. Wang, J. Shi, Recrystallization behavior and tensile properties of laser metal deposited inconel 718 upon in-situ ultrasonic impact peening and heat treatment, Mater. Sci. Eng. 786 (2020) 139434, https://doi.org/10.1016/j.msea.2020.139434.
[44] Q. Chen, G. Wang, H. Zhang, R. Li, Research on microstructure and mechanical properties of hybrid plasma arc and micro-rolling additive manufacturing of inconel 718 superalloy, Rapid Prototyp. J. 28 (2022) 1509–1519, https://doi.org/10.1108/rpj-09-2021-0227.
[45] J.R. Hönnige, A.E. Davis, A. Ho, J.R. Kennedy, L. Neto, P. Prangnell, S. Williams, The effectiveness of grain refinement by machine hammer peening in high deposition rate wire-arc AM Ti-6Al-4V, Metall. Mater. Trans. 51 (2020) 3692–3703, https://doi.org/10.1007/s11661-020-05781-6.
[46] V.R. Duarte, T.A. Rodrigues, N. Schell, R.M. Miranda, J.P. Oliveira, T.G. Santos, In-situ hot forging direct energy deposition-arc of CuAl8 alloy, Addit. Manuf. (2022) 102847, https://doi.org/10.1016/j.addma.2022.102847.
[47] J. Hönnige, C.E. Seow, S. Ganguly, X. Xu, S. Cabeza, H. Coules, S. Williams, Study of residual stress and microstructural evolution in as-deposited and inter-pass rolled wire plus arc additively manufactured inconel 718 alloy after ageing treatment, Mater. Sci. Eng. 801 (2021) 140368, https://doi.org/10.1016/j.msea.2020.140368.
[48] C. Li, Y. Tian, Y. Chen, P. Hodgson, X. Wu, Y. Zhu, A. Huang, Hierarchical layered and refined grain structure of inconel 718 superalloy produced by rolling-assisted directed energy deposition, Addit. Manuf. Lett. 1 (2021) 100009, https://doi.org/10.1016/j.addlet.2021.100009.
[49] B. Parvaresh, R. Miresmaeili, M. Yazdizadeh, Characterization of wire arc additive manufactured products: a comparison between as-deposited and inter-layer cold worked specimens, J. Manuf. Process. 57 (2020) 61–71, https://doi.org/10.1016/j.jmapro.2020.05.053.
[50] Q. Li, Y. Zhang, J. Chen, B. Guo, W. Wang, Y. Jing, Y. Liu, Effect of ultrasonic micro-forging treatment on microstructure and mechanical properties of GH3039 superalloy processed by directed energy deposition, J. Mater. Sci. Technol. 70 (2021) 185–196, https://doi.org/10.1016/j.jmst.2020.09.001.
[51] B. Lan, Y. Wang, Y. Liu, P. Hooper, C. Hopper, G. Zhang, X. Zhang, J. Jiang, The influence of microstructural anisotropy on the hot deformation of wire arc additive manufactured (WAAM) inconel 718, Mater. Sci. Eng. 823 (2021) 141733, https://doi.org/10.1016/j.msea.2021.141733.
[52] R. Hielscher, H. Schaeben, A novel pole figure inversion method: specification of the MTEX algorithm, J. Appl. Crystallogr. 41 (2008) 1024–1037, https://doi.org/10.1107/S0021889808030112.
[53] A.P. Hammersley, S.O. Svensson, M. Hanfland, A.N. Fitch, D. Häusermann, Two-dimensional detector software: from real detector to idealised image or two-theta scan, High Press. Res. 14 (1996) 235–248, https://doi.org/10.1080/08957959608201408.
[54] P. Crowther, C.S. Daniel, Xrdfit: a python package for fitting synchrotron X-ray diffraction spectra, J. Open Source Softw. 5 (2020) 2381, https://doi.org/10.21105/joss.02381.
[55] X. Xu, J. Ding, S. Ganguly, S. Williams, Investigation of process factors affecting mechanical properties of INCONEL 718 superalloy in wire + arc additive manufacture process, J. Mater. Process. Technol. 265 (2019) 201–209, https://doi.org/10.1016/j.jmatprotec.2018.10.023.
[56] H. Zhang, X. Wang, G. Wang, Y. Zhang, Hybrid direct manufacturing method of metallic parts using deposition and micro continuous rolling, Rapid Prototyp. J. 19 (2013) 387–394, https://doi.org/10.1108/RPJ-01-2012-0006.
[57] M. Schneider, J.P. Couzinié, A. Shalabi, F. Ibrahimkhel, A. Ferrari, F. Körmann, G. Laplanche, Effect of stacking fault energy on the thickness and density of annealing twins in recrystallized FCC medium and high-entropy alloys, Scr. Mater. 240 (2024) 115844, https://doi.org/10.1016/j.scriptamat.2023.115844.
[58] A. Nicolaÿ, J.M. Franchet, J. Cormier, H. Mansuor, M. De Graef, A. Seret, N. Bozzolo, Discrimination of dynamically and post-dynamically recrystallized grains based on EBSD data: application to inconel 718, J. Microsc. 273 (2019) 135–147, https://doi.org/10.1111/jmi.12769.
[59] S.-S. Rui, Y.-B. Shang, W. Qiu, L.-S. Niu, H.-J. Shi, S. Matsumoto, Y. Chuman, Fracture mode identification of low alloy steels and cast irons by electron back-scattered diffraction misorientation analysis, J. Mater. Sci. Technol. 33 (2017) 1582–1595, https://doi.org/10.1016/j.jmst.2017.03.020.
[60] A.R. McAndrew, M. Alvarez Rosales, P.A. Colegrove, J.R. Hönnige, A. Ho, R. Fayolle, K. Eyitayo, I. Stan, P. Sukrongpang, A. Crochemore, Z. Pinter, Interpass rolling of Ti-6Al-4V wire + arc additively manufactured features for microstructural refinement, Addit. Manuf. 21 (2018) 340–349, https://doi.org/10.1016/j.addma.2018.03.006.
[61] A. Rollett, F.J. Humphreys, G.S. Rohrer, M. Hatherly, Recrystallization and Related Annealing Phenomena, second ed., Elsevier Ltd, 2017 https://doi.org/10.1016/B978-0-08-098235-9.00001-X.
[62] B. Radhakrishnan, G.B. Sarma, T. Zacharia, Modeling the kinetics and microstructural evolution during static recrystallization—Monte carlo simulation of recrystallization, Acta Mater. 46 (1998) 4415–4433, https://doi.org/10.1016/S1359-6454(98)00077-9.
[63] T.S. Prithiv, P. Bhuyan, S.K. Pradhan, V. Subramanya Sarma, S. Mandal, A critical evaluation on efficacy of recrystallization vs. strain induced boundary migration in achieving grain boundary engineered microstructure in a Ni-base superalloy, Acta Mater. 146 (2018) 187–201, https://doi.org/10.1016/j.actamat.2017.12.045.
[64] J.C. Dutra, R.H. Gonçalves e Silva, K.C. Riffel, C. Marques, High-performance GMAW process for deep penetration applications, Weld. World 64 (2020) 999–1009, https://doi.org/10.1007/s40194-020-00889-0.
[65] S. Gao, R. Liu, R. Huang, X. Song, M. Seita, A hybrid directed energy deposition process to manipulate microstructure and properties of austenitic stainless steel, Mater. Des. 213 (2022) 110360, https://doi.org/10.1016/j.matdes.2021.110360.

[66] X.F. Fan, J. Zhou, C.J. Qiu, B. He, J. Ye, B. Yuan, Z. Pi, Experimental study on surface characteristics of laser cladding layer regulated by high-frequency microforging, J. Therm. Spray Technol. 20 (2011) 456–464, https://doi.org/10.1007/s11666-010-9534-8.

[67] P. Dirisu, G. Supriyo, F. Martina, X. Xu, S. Williams, Wire plus arc additive manufactured functional steel surfaces enhanced by rolling, Int. J. Fatig. 130 (2020) 105237, https://doi.org/10.1016/j.ijfatigue.2019.105237.

[68] J.V. Gordon, C.V. Haden, H.F. Nied, R.P. Vinci, D.G. Harlow, Fatigue crack growth anisotropy, texture and residual stress in austenitic steel made by wire and arc additive manufacturing, Mater. Sci. Eng. 724 (2018) 431–438, https://doi.org/10.1016/j.msea.2018.03.075.

[69] H.L. Wei, J. Mazumder, T. DebRoy, Evolution of solidification texture during additive manufacturing, Sci. Rep. 5 (2015) 16446, https://doi.org/10.1038/srep16446.

[70] L. Ling, Y. Han, W. Zhou, H. Gao, D. Shu, J. Wang, M. Kang, B. Sun, Study of microsegregation and laves phase in INCONEL718 superalloy regarding cooling rate during solidification, Metall. Mater. Trans. 46 (2015) 354–361, https://doi.org/10.1007/s11661-014-2614-5.

[71] D. Van, G.P. Dinda, J. Park, J. Mazumder, S.H. Lee, Enhancing hardness of inconel 718 deposits using the aging effects of cold metal transfer-based additive manufacturing, Mater. Sci. Eng. 776 (2020) 139005, https://doi.org/10.1016/j.msea.2020.139005.

[72] C.C. Silva, H.C. de Miranda, M.F. Motta, J.P. Farias, C.R.M. Afonso, A.J. Ramirez, New insight on the solidification path of an alloy 625 weld overlay, J. Mater. Res. Technol. 2 (2013) 228–237, https://doi.org/10.1016/j.jmrt.2013.02.008.

[73] M. Solecka, A. Kopia, A. Radziszewska, B. Rutkowski, Microstructure, microsegregation and nanohardness of CMT clad layers of Ni-base alloy on 16Mo3 steel, J. Alloys Compd. 751 (2018) 86–95, https://doi.org/10.1016/j.jallcom.2018.04.102.

[74] Y. Kong, K. Peng, H. Huang, Highly controllable additive manufacturing of heterostructured nickel-based composites, Int. J. Mach. Tool Manufact. 195 (2024) 104112, https://doi.org/10.1016/j.ijmachtools.2023.104112.

[75] S.A. Oh, R.E. Lim, J.W. Aroh, A.C. Chuang, B.J. Gould, J. V Bernier, N. Parab, T. Sun, R.M. Suter, A.D. Rollett, Microscale observation via high-speed X-ray diffraction of alloy 718 during in situ laser melting, J. Occup. Med. 73 (2021) 212–222, https://doi.org/10.1007/s11837-020-04481-1.

[76] G.A. Knorovsky, M.J. Cieslak, T.J. Headley, A.D. Romig, W.F. Hammetter, Inconel 718: a solidification diagram, Metall. Trans. A 20 (1989) 2149–2158, https://doi.org/10.1007/BF02650300.

[77] J.N. Dupont, C.V. Robino, A.R. Marder, M.R. Notis, Solidification of Nb-bearing superalloys: part II. Pseudoternary solidification surfaces, Metall. Mater. Trans. 29 (1998) 2797–2806, https://doi.org/10.1007/S11661-998-0320-X.

[78] J.J. Ruan, N. Ueshima, K. Oikawa, Phase transformations and grain growth behaviors in superalloy 718, J. Alloys Compd. 737 (2018) 83–91, https://doi.org/10.1016/j.jallcom.2017.11.327.

[79] A. Prasad, L. Yuan, P. Lee, M. Patel, D. Qiu, M. Easton, D. StJohn, Towards understanding grain nucleation under additive manufacturing solidification conditions, Acta Mater. 195 (2020) 392–403, https://doi.org/10.1016/j.actamat.2020.05.012.

[80] S. Zhang, X. Lin, L. Wang, X. Yu, Y. Hu, H. Yang, L. Lei, W. Huang, Strengthening mechanisms in selective laser-melted Inconel718 superalloy, Mater. Sci. Eng. 812 (2021) 141145, https://doi.org/10.1016/j.msea.2021.141145.

[81] S. Sui, H. Tan, J. Chen, C. Zhong, Z. Li, W. Fan, A. Gasser, W. Huang, The influence of laves phases on the room temperature tensile properties of inconel 718 fabricated by powder feeding laser additive manufacturing, Acta Mater. 164 (2019) 413–427, https://doi.org/10.1016/J.ACTAMAT.2018.10.032.

[82] E. Hosseini, V.A. Popovich, A review of mechanical properties of additively manufactured inconel 718, Addit. Manuf. 30 (2019) 100877, https://doi.org/10.1016/j.addma.2019.100877.

[83] K. Wang, Y. Liu, Z. Sun, J. Lin, Y. Lv, B. Xu, Microstructural evolution and mechanical properties of inconel 718 superalloy thin wall fabricated by pulsed plasma arc additive manufacturing, J. Alloys Compd. 819 (2020) 152936, https://doi.org/10.1016/J.JALLCOM.2019.152936.

[84] S. Sui, Z. Li, C. Zhong, Q. Zhang, A. Gasser, J. Chen, Y. Chew, G. Bi, Laves phase tuning for enhancing high temperature mechanical property improvement in laser directed energy deposited inconel 718, Composites, Part B 215 (2021) 108819, https://doi.org/10.1016/j.compositesb.2021.108819.

[85] S.H. Sun, Y. Koizumi, T. Saito, K. Yamanaka, Y.P. Li, Y. Cui, A. Chiba, Electron beam additive manufacturing of inconel 718 alloy rods: impact of build direction on microstructure and high-temperature tensile properties, Addit. Manuf. 23 (2018) 457–470, https://doi.org/10.1016/J.ADDMA.2018.08.017.

[86] Q. Teng, S. Li, Q. Wei, Y. Shi, Investigation on the influence of heat treatment on inconel 718 fabricated by selective laser melting: microstructure and high temperature tensile property, J. Manuf. Process. 61 (2021) 35–45, https://doi.org/10.1016/j.jmapro.2020.11.002.

[87] T. Trosch, J. Strößner, R. Völkl, U. Glatzel, Microstructure and mechanical properties of selective laser melted inconel 718 compared to forging and casting, Mater. Lett. 164 (2016) 428–431, https://doi.org/10.1016/J.MATLET.2015.10.136.

[88] M.S. Dodaran, S. Guo, M.M. Khonsari, N. Shamsaei, S. Shao, A theoretical calculation of stacking fault energy of Ni alloys: the effects of temperature and composition, Comput. Mater. Sci. 191 (2021) 110326, https://doi.org/10.1016/j.commatsci.2021.110326.

[89] F. HajyAkbary, J. Sietsma, A.J. Böttger, M.J. Santofimia, An improved X-ray diffraction analysis method to characterize dislocation density in lath martensitic structures, Mater. Sci. Eng. 639 (2015) 208–218, https://doi.org/10.1016/j.msea.2015.05.003.

[90] T. Seymour, P. Frankel, L. Balogh, T. Ungár, S.P. Thompson, D. Jädernäs, J. Romero, L. Hallstadius, M.R. Daymond, G. Ribárik, M. Preuss, Evolution of dislocation structure in neutron irradiated Zircaloy-2 studied by synchrotron x-ray diffraction peak profile analysis, Acta Mater. 126 (2017) 102–113, https://doi.org/10.1016/j.actamat.2016.12.031.

[91] A. Borbély, The modified williamson-hall plot and dislocation density evaluation from diffraction peaks, Scr. Mater. 217 (2022) 114768, https://doi.org/10.1016/j.scriptamat.2022.114768.

[92] D.M. Dimiduk, M.D. Uchic, T.A. Parthasarathy, Size-affected single-slip behavior of pure nickel microcrystals, Acta Mater. 53 (2005) 4065–4077, https://doi.org/10.1016/j.actamat.2005.05.023.

[93] J.E. Bailey, P.B. Hirsch, The dislocation distribution, flow stress, and stored energy in cold-worked polycrystalline silver, Philos. Mag. A J. Theor. Exp. Appl. Phys. 5 (2006) 485–497, https://doi.org/10.1080/14786436008238300.

[94] J.M. Oblak, D.S. Duvall, D.F. Paulonis, An estimate of the strengthening arising from coherent, tetragonally-distorted particles, Mater. Sci. Eng. 13 (1974) 51–56, https://doi.org/10.1016/0025-5416(74)90020-2.

[95] E.I. Galindo-Nava, L.D. Connor, C.M.F. Rae, On the prediction of the yield stress of unimodal and multimodal γ′ nickel-base superalloys, Acta Mater. 98 (2015) 377–390, https://doi.org/10.1016/j.actamat.2015.07.048.

[96] J.M. Oblak, D.F. Paulonis, D.S. Duvall, Coherency strengthening in Ni base alloys hardened by DO22 γ′ precipitates, Metall. Trans. A 5 (1974) 143–153, https://doi.org/10.1007/BF02642938.

[97] W.F. Hosford, The Mechanics of Crystals and Textured Polycrystals, first ed., Oxford University Press, 1993.

[98] S. Birosca, F. Di Gioacchino, S. Stekovic, M. Hardy, A quantitative approach to study the effect of local texture and heterogeneous plastic strain on the deformation micromechanism in RR1000 nickel-based superalloy, Acta Mater. 74 (2014) 110–124, https://doi.org/10.1016/j.actamat.2014.04.039.

[99] J. Liang, Z. He, W. Du, X. Ruan, E. Guo, N. Shen, Tailoring the microstructure and mechanical properties of laser metal-deposited hastelloy X superalloy sheets via post heat-treatment, Mater. Sci. Eng. 884 (2023) 145546, https://doi.org/10.1016/j.msea.2023.145546.

[100] M. Sazerat, A. Nait-Ali, A. Cervellon, I. Lopez-Galilea, G. Burlot, S. Gillet, D. Eyidi, A. Joulain, P. Villechaise, S. Weber, R. Fortunier, J. Cormier, High temperature microstructure stability of waspaloy produced by wire arc additive manufacturing, J. Alloys Compd. 966 (2023) 171626, https://doi.org/10.1016/j.jallcom.2023.171626.

[101] S. Li, Q. Wei, Y. Shi, Z. Zhu, D. Zhang, Microstructure characteristics of inconel 625 superalloy manufactured by selective laser melting, J. Mater. Sci. Technol. 31 (2015) 946–952, https://doi.org/10.1016/j.jmst.2014.09.020.

[102] C. Kumara, D. Deng, J. Moverare, P. Nylén, Modelling of anisotropic elastic properties in alloy 718 built by electron beam melting, Mater. Sci. Technol. 34 (2018) 529–537, https://doi.org/10.1080/02670836.2018.1426258.

[103] P. Baudoin, V. Magnier, A. El Bartali, J.-F. Witz, P. Dufrenoy, F. Demilly, É. Charkaluk, Numerical investigation of fatigue strength of grain size gradient materials under heterogeneous stress states in a notched specimen, Int. J. Fatig. 87 (2016) 132–142, https://doi.org/10.1016/j.ijfatigue.2016.01.022.

[104] B. Zhang, A.F. Quiñonez, C.H. Venner, Effect of material anisotropy on rolling contact fatigue life under dry and lubricated point contact conditions: a numerical study, Tribol. Int. 152 (2020) 106584, https://doi.org/10.1016/j.triboint.2020.106584.

[105] F.W.C. Farias, V.R. Duarte, J. da C. Payão Filho, T.J.G. dos Santos, J.P. Oliveira, An overview of Ni-based superalloy 718 fabricated via arc-based directed energy deposition, J. Manuf. Process. 149 (2025) 892–916, https://doi.org/10.1016/j.jmapro.2025.06.005.

[106] Y. Chen, C. Yang, C. Fan, M. Wang, The influence of solution temperature on microstructure evolution and mechanical properties of ATI 718Plus repaired by wire and arc additive manufacturing, Mater. Sci. Eng. 852 (2022) 143641, https://doi.org/10.1016/j.msea.2022.143641.

[107] V.R. Duarte, Developments in directed energy deposition additive manufacturing: in-situ hot forging and indirect cooling, Universidade NOVA de Lisboa (2022). https://run.unl.pt/handle/10362/134198. (Accessed 19 April 2022).